Arany, L., Bhattacharya, S., Macdonald, J. H. G., & Hogan, S. J. (2015). Simplified critical mudline bending moment spectra of offshore wind turbine support structures. Wind Energy, 18(12), 2171-2197. 10.1002/we.1812

Simplified critical mudline bending moment spectra of offshore wind turbine support structures

László Arany[1], Subhamoy Bhattacharya[2], John Macdonald[3], S. John Hogan[4]

[1] Research Scholar, University of Bristol
[2] Professor, University of Surrey
[3] Reader, University of Bristol
[4] Professor, University of Bristol

Corresponding author:
László Arany
Research Scholar,
University of Bristol
Email: laszlo.arany@bristol.ac.uk
Phone number: +44 7423 690 220
Website:

Abstract:

Offshore wind turbines are subjected to multiple dynamic loads arising from the wind, waves, rotational frequency (1P) and the blade passing frequency (3P) loads. In the literature, these loads are often represented using a frequency plot where the Power Spectral Densities (PSDs) of wave height and wind turbulence are plotted against the corresponding frequency range. The PSD magnitudes are usually normalised to unity, probably because they have different units and thus the magnitudes are not directly comparable. In this paper a generalised attempt has been made to evaluate the relative magnitudes of these four loadings by transforming them to bending moment spectra using site and turbine specific data. A formulation is proposed to construct bending moment spectra at the mudline, i.e. at the location where the highest fatigue damage is expected. Equally, this formulation can also be tailored to find the bending moment at any other critical cross section, e.g. the Transition Piece (TP) level. Finally, an example case study is considered to demonstrate the application of the proposed methodology. The constructed spectra serve as a basis for frequency based fatigue estimation methods available in the literature.

Keywords: offshore wind turbine, wind loading, wave loading, natural frequency, rotor imbalance, blade passage, power spectral density, fatigue damage

Nomenclature

A_P	pile cross section area (area of the outer circle) ($A_P = D_P^2\pi/4$)
A_R	rotor area
b	rotor overhang (distance from the axis of the wind turbine tower to the centre of the hub)
B_{root}	blade root chord lenth
B_{tip}	blade tip chord length
C_a	added mass coefficient
C_D	drag coefficient
C_m	inertia coefficient
C_T	thrust coefficient
d	characteristic size of eddies
D	rotor diameter of the turbine
D_{lower}	diameter of the tower at the height of the blade tip when the blade is in its downward vertical position
D_{top}	tower top diameter
D_P	diameter of the monopile (assumed equal to the diameter of the transition piece)
D_T	diameter of the tower
f	frequency
f_{1P}	frequency of the rotation of the rotor
f_{3P}	blade passing frequency of 3-bladed wind turbines
f_p	peak frequency of spectra
F	fetch (distance from a leeward shore)
F_{cf}	centrifugal force
F_D	drag force
F_I	lateral force due to inertial forces (function of time and space)
$F_{I,max}$	maximum of the lateral inertia forces
F_T	total lateral force from waves
$F_{T,max}$	maximum of the total lateral force from waves
g	gravitational acceleration, $g = 9.81\ [m/s^2]$
H	hub height above Mean Sea Level (MSL)
$H_{1/3}$	significant wave height (average of the highest one third of waves)
I	turbulence intensity
I_m	mass imbalance parameter of the rotor $I_m = mR$
k	wave number of ocean waves ($k = 2\pi/\lambda$)
K_C	Kreulegan-Carpenter number
L	length of the blades
L_k	horizontal integral length scale
m	mass of the imbalance of the rotor
M_{1P}	maximum of the total 1P fore-aft bending moment at mudline
M_{drag}	moment from drag force on the tower from wind
$M_{I,max}$	maximum of the fore-aft bending moment at mudline due to inertia forces
$M_{T,max}$	maximum of the total fore-aft bending moment at mudline level due to waves
M_T	total fore-aft moment at mudline from waves
$M_{towertop}$	bending moment from wind drag on the top part of the tower (i.e. the part covered by the passing blade)
M_y	maximum of the fore-aft bending moment at mudline due to mass imbalance of the rotor
MSL	Mean Sea Level
r	peak enhancement exponent (JONSWAP)
R	radial position of the imbalance
R_A	ratio of the face area of the blade and the area of the top part of the tower
S	mean sea depth (equals to mean sea level)
$S_{uu}(f)$	Kaimal horizontal wind spectrum
$\tilde{S}_{uu}(f)$	normalised Kaimal spectrum of horizontal wind speed
$S_{ww}(f)$	JONSWAP spectrum of wave height
$S_{FF,wind}(f)$	spectral density function of the thrust force acting on the hub from wind turbulence
$S_{MM,wind}(f)$	spectral density function of the fore-aft bending moment at mudline due to the thrust force on the hub from wind turbulence
$S_{MM,wave}(f)$	spectral density of the fore-aft bending moment at mudline due to waves
$S_{MM,1P}(f)$	spectral density of the fore-aft bending moment from 1P loads
$S_{MM,3P}(f)$	spectral density of the fore-aft bending moment from 3P loads
T	cycle period
T_p	peak time period of waves
Th	thrust force
TP	Transition Piece (the element connecting the turbine tower to the monopile of the foundation)
u	fluctuating component of wind speed
$u(t)$	instantaneous horizontal velocity of water particles
$\dot{u}(t)$	instantaneous horizontal acceleration of water particles
u_{max}	maximum of the horizontal component of the velocity of water particles $u(x,t)$
U	wind speed
$\overline{U}$	mean wind speed
x	vertical coordinate along the axis of the tower with zero at Mean Sea Level (MSL)
y	horizontal coordinate in the side-to-side direction
z	horizontal coordinate in the fore-aft direction
z_0	surface roughness
α	intensity of the spectrum (JONSWAP)
β	wind profile exponent
γ	peak enhancement factor (JONSWAP)
$\gamma_{wind}/\gamma_{wave}$	safety factors (load factors) for wind/waves
δ	Dirac-delta function
$\langle\zeta^2\rangle$	variance of the surface displacement
$\eta(z,t)$	surface elevation
θ	azimuthal position of the imbalance
ϑ	instantaneous phase
λ	wavelength of ocean waves
ρ_a	density of air
ρ_w	density of sea water
σ	JONSWAP parameter
σ_U	standard deviation of wind speed
τ	rotor crossing time interval
φ	rotor position; angle of Blade I and the upward vertical direction
$\chi(f)$	Aerodynamic Admittance Function (AAF)
ω	angular frequency of waves
Ω	rotational speed of the rotor

1. Introduction

Offshore wind turbines (OWTs), due to their shape and form (slender column with a heavy mass as well as a rotating mass at the top) are dynamically sensitive [1] [2] [3], because the natural frequency of these slender structures are very close to the excitation frequencies imposed by the environmental and mechanical loads. The main dynamic loads acting on the wind turbine are as follows: (a) The load produced by the turbulence in the wind, the magnitude of which depends on the turbulent wind speed; (b) The load caused by waves crashing against the substructure, the magnitude of which depends on the wave height and wave period; (c) Load caused by the vibration at the hub level due to the mass and aerodynamic imbalances of the rotor. This load has a frequency equal to the rotational frequency of the rotor (referred to as 1P loading in the literature). Since most of the industrial wind turbines are variable speed machines, 1P is not a single frequency but a frequency band between the frequencies associated with the lowest and the highest rpm (revolutions per minute); (d) Loads in the tower due to the vibrations caused by blade shadowing effects (referred to as 2P/3P in the literature). The blades of the wind turbine passing in front of the tower cause a shadowing effect and produce a loss of wind load on the tower. This is a dynamic load having frequency equal to three times the rotational frequency of the turbine (3P) for three bladed wind turbines and two times (2P) the rotational frequency of the turbine for a two bladed turbine. The 2P/3P loading is also a frequency band like 1P and is simply obtained by multiplying the limits of the 1P band by the number of the turbine blades.

Figure 1 shows the main frequencies described above from a three-bladed Siemens 3.6MW wind turbine having a rotational operating interval of 5-13 RPM (lowest is 5RPM i.e. 0.083Hz and highest is 13RPM i.e. 0.216Hz). A mean wind speed of 9 m/s, fetch of 60km and a peak wave frequency of 0.197Hz are used to construct the dynamic spectra.

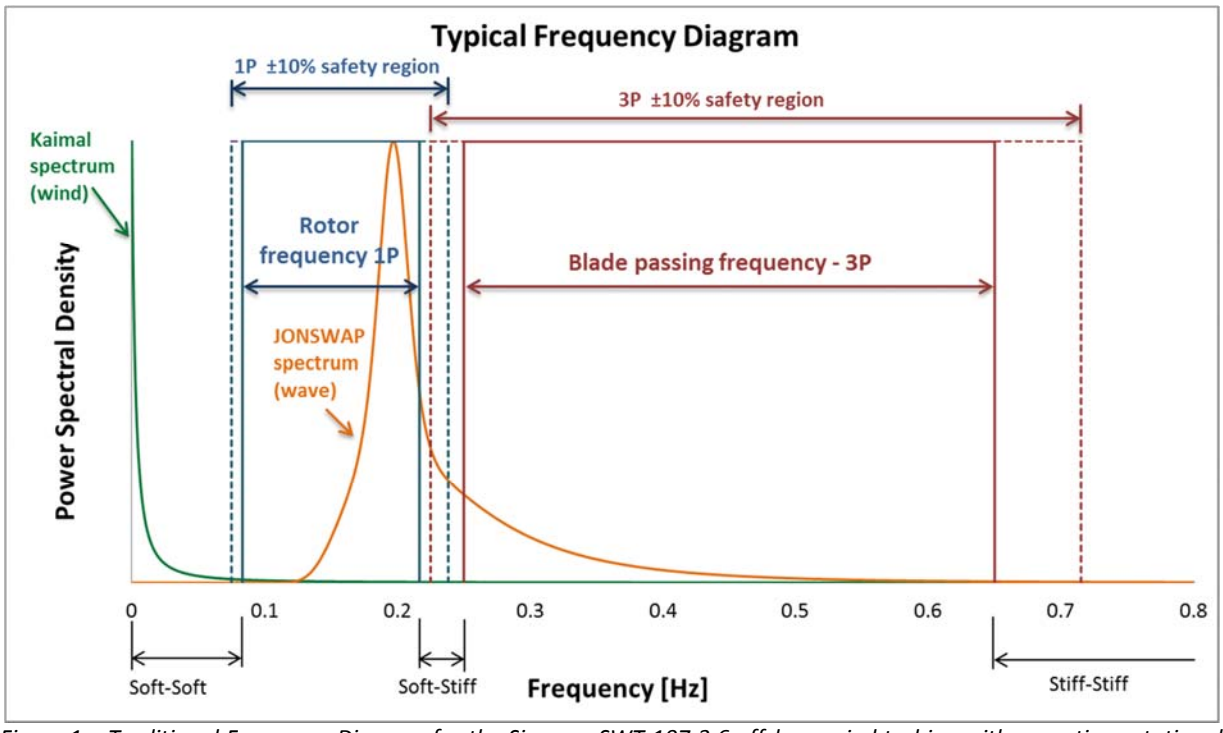

Figure 1 – Traditional Frequency Diagram for the Siemens SWT-107-3.6 offshore wind turbine with operating rotational wind speed range between 5-13rpm (using the mean wind speed U=9m/s and fetch F=60km. The frequency diagram includes Wind Spectrum, Wave Spectrum, 1P and 3P frequency bands. The amplitudes are normalised to unity to focus on the frequency content of the loading.

The turbulent wind velocity and the wave height on sea are both variables and are best treated statistically using Power Spectral Density (PSD) functions. In other words, instead of time domain analysis the produced loads are more effectively analysed in the frequency domain whereby the contribution of each frequency to the total power in wind turbulence and in ocean waves is described. Representative wave and wind (turbulence) spectra can be constructed by a Discrete Fourier Transform [4], [5] from site specific data. However, in absence of such data, theoretical spectra can also be used. The DNV standard [6] specifies the Kaimal spectrum for wind and the JONSWAP (Joint North Sea Wave Project) spectrum for waves in offshore wind turbine applications. Figure 1 plots the PSD function for the wind and wave using a mean wind speed of 9m/s and fetch of 60km. The figure also shows the 1P and 3P frequency bands. It is clear from the frequency content of the applied loads (see Figure 1) that the designer has to select a system frequency (the global frequency of the overall wind turbine including the foundation) which lies outside these frequencies to avoid resonance and ultimately increased fatigue damage. From the point of view of first natural frequency f_0 of the structure, three types of designs are possible (see Figure 1):

(1) *Soft-Soft* design where f_0 is placed below the 1P frequency range $\left(f_0 < f_{1P,min}\right)$ which is a very flexible structure and almost impossible to design for a grounded system.

(2) *Soft-Stiff* design where f_0 is between 1P and 3P frequency ranges $\left(f_{1P,max} < f_0 < f_{3P,min}\right)$ and this is the most common in the current offshore development.

(3) *Stiff-Stiff* designs where f_0 have a higher natural frequency than the upper limit of the 3P band $\left(f_0 > f_{3P,max}\right)$ and will need a very stiff support structure.

It is of interest to review the codes of practice in this regard. DNV code [7] suggests that first natural frequency should not be within 10% of the 1P and 3P ranges as indicated in Figure 1. It is apparent from Figure 1 that the first natural frequency of the wind turbine needs to be fitted in a very narrow band (in some cases the 1P and 3P ranges may even coincide leaving no gap). It is important to note, as pointed out in [8] that from the point of view of dynamics, OWT designs are only conservative if the prediction of the first natural frequency is accurate. Unlike in the case of some other offshore structures (such as the ones used in the oil and gas industry), under-prediction of f_0 is unconservative. The safest solution would seem to be placing the natural frequency of the wind turbine well above the 3P range. However, stiffer designs with higher natural frequency require massive support structures and foundations involving higher costs of materials, transportation and installation. Thus from an economic point of view, softer structures are desirable and it is not surprising that almost all of the installed wind turbines are "soft-stiff" designs and this type is expected to be used in the future as well. It is clear from the above discussion that designing soft-stiff wind turbine systems demands the consideration of dynamic amplification and also any potential change in system frequency due to the effects of cyclic/dynamic loading on the system i.e. Dynamic-Structure-Foundation-Soil-Interaction. Typically the first modal frequency of the wind turbine system lies in the range of 75% to 120% of the excitation frequencies and as a result, dynamic amplifications of responses are expected. (For example, referring to Figure 1, the natural frequency of a Siemens SWT-3.6-107 turbine at the Walney 1 site is estimated at $f_n = 0.335Hz$. The upper limit of the 1P frequency band is $f_{1P,max} = 0{,}217Hz$ and the lower limit of the 3P band is $f_{3P,min} = 0.25Hz$, the upper limit of 3P is $f_{3P,max} = 0.65Hz$. Similar numbers are typical for other existing wind turbines as well. The calculated frequency ratios are 65% for the upper limit of 1P, 75% for the lower limit of 3P running through to the upper limit of 194%. Wave loading typically has significant power in the 0.05-0.5Hz range, and the wind load has a 1P and 3P component as well.)

Recent research [1][2][3],[9][10][11][12] on the long term performance of wind turbine systems due to dynamic soil structure interaction arrived at the following conclusions:

(a) The change in natural frequencies of the wind turbine system may be affected by the choice of foundation system i.e. deep foundation or multiple pods on shallow foundations. Deep foundations such as monopiles will exhibit sway-bending mode i.e. the first two modes are widely spaced. However multiple pod foundations supported on shallow foundations (such as tetrapod or tripod on suction caisson) will exhibit rocking modes in two principle planes.

(b) The natural frequencies of wind turbine systems change with repeated cyclic/dynamic loading. In the case of strain-hardening site (such as loose to medium dense sandy site) the natural frequency is expected to increase and for strain-softening site (such as normally consolidated clay) the natural frequency will decrease.

(c) Due to rocking modes of vibration, there will be a 'two-peak' response i.e. two closely spaced frequencies for multipod foundations (tripod/tetrapod).

Clearly, for soft-stiff design, any change in natural frequency will enhance the dynamic amplifications which will increase the vibration amplitudes and thus the stresses and fatigue damage on the structure. It must be mentioned in this context that it was reported in [13] that the fatigue load from waves increased by 300% by assuming a softer support structure. Therefore fatigue is one of the design drivers for these structures. Predicting fatigue damage is undoubtedly a formidable task due to complexity associated with the uncertainty in the dynamic amplification (owing to changes in system characteristics over time and number of cycles), randomness of the environmental loading and last but not the least, the impact of climate change.

Offshore wind turbines are currently being installed in high numbers around Europe and their role in electricity production is expected to increase in the following decades. To make offshore wind farm investments worthwhile, it is necessary to ensure that they are operational throughout their intended design lifetime. Since any a posteriori change to these structures involves very high costs due to the complexity of the maintenance processes and due to low availability of suitable vessels, it is essential to design wind farms carefully such that the fatigue damage is kept low to achieve the longest possible service lifetime.

The aim of the paper is therefore to develop a framework to compute bending moment spectra at critical locations from the point of view of fatigue damage. This can be later used for quick fatigue damage estimation. The paper is structured in the following way. Section 2 begins by discussing the complexity of the dynamic loading from the wind, wave, 1P and 3P loadings. The frequency diagrams often used ([1], [2], [10], [14]) in codes of practice for wind and wave loading are critically reviewed as they do not contain all the necessary information about the nature of the loading. This section also highlights the shortcomings of the simple frequency diagram representation shown in Figure 1. The expression for bending moment spectra at the mudline for each of the four types of loading are then presented. Section 3 shows the application of the derived methodology using the Siemens turbines at the Walney offshore wind farm site and the critical bending moment spectra are plotted.

2. Complexity of loading and bending moment spectra

It may be noted that in Figure 1 the magnitudes of the spectral densities are normalised to 1. However, it is considered useful for the decision making process if the magnitudes of these PSDs are comparable. In this paper an attempt has been made to construct useful spectra whereby these loads could be compared. The effects from the major loads are transformed to bending moments at the mudline (seabed) in the fore-aft direction of the structure, where the highest mudline bending moments are expected. In this paper, the turbulent wind load is taken into consideration through the use of the Kaimal spectrum [6], [15] and the wave loading through the JONSWAP spectrum [16]. The simplifications and limitations introduced by these spectra are detailed for wind and wave spectrum in Section 2.1 and Section 2.3, respectively. It is to be noted here that these spectra are used as examples and they are chosen based on suggestions by standards used in the industry ([6], [17]–[19]). The methodology presented, however, is not limited to these spectra and any other theoretical or custom site specific spectra can also be used. Addressing the 1P loading effect is a challenging task, in this paper typical values of mass imbalance is assumed based on the literature [20], [21] to estimate the effects at the mudline. The dynamic loading effects due to blade passage (3P loading) is estimated by a simple geometric expression of the drag load loss on the tower.

The next section derives the necessary formulation for the bending moment spectra.

2.1 Wind loading

It is usual to treat the turbulence in the wind as a fluctuating wind speed component (u) superimposed on the mean wind speed $\overline{U}$, thus the total wind speed is written as $U = \overline{U} + u$. The strength of turbulence is usually characterised by the turbulence intensity I [19], given by Equation 1.

$$I = \sigma_U / \overline{U} \tag{1}$$

where σ_U is the standard deviation of wind speed around the mean $\overline{U}$ (which is usually taken over 10 minutes). The turbulence intensity varies with mean wind speed, with site location and with surface roughness, and it is also modified by the turbine itself.

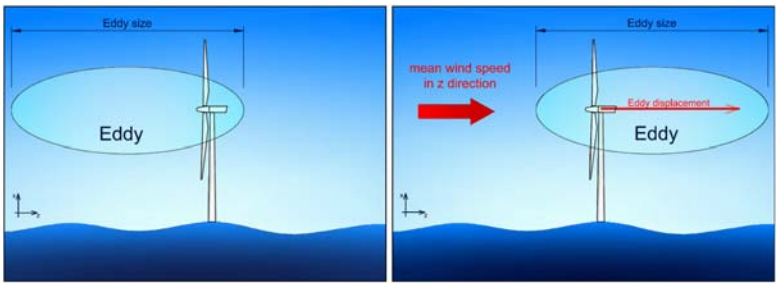

Figure 2 – Taylor's frozen turbulence hypothesis: an eddy travels with the mean wind speed while its size and characteristic parameters remain constant.

Taylor's frozen turbulence hypothesis [22] is assumed in this paper, that is, that the characteristics of eddies can be considered constant (frozen) in time, and vortices travel with the mean horizontal wind speed as shown in Figure 2. This assumption was found to be acceptable for wind turbine applications [23]. Wind turbulence is usually analysed in the frequency domain by a power spectral density (PSD) function, which describes the contribution of different frequencies to the total variance of the wind speed. The frequency of turbulence is connected to the size of eddies, a larger eddy means low frequency variation in wind speed, while smaller vortices induce short, high frequency wind speed variations. If an eddy's characteristic size is $d[m]$ and it travels with $\overline{U}[m/s]$ speed, then it travels through the rotor in $\tau = d/\overline{U}$ time. The frequency connected to this time period is $f = 1/\tau[Hz]$.

This way the length scale and time scale of turbulence are connected. The typical length scales of high energy-containing large turbulent eddies are in the range of several kilometres. The large eddies tend to decay to smaller and smaller eddies with higher frequencies as turbulent energy dissipates to heat. Kolmogorov's law describing this process and states that the asymptotic limit of the spectrum is $f^{-5/3}$ at high frequency [15]. There are two families of spectra commonly used in wind energy applications, the von Kármán and the Kaimal spectra, the main difference being that the Kaimal spectrum is somewhat less peaked and the energy is contained in a bit wider frequency range. According to [24], the Kaimal spectrum is more suitable for modelling the atmospheric boundary layer, and the von Karman spectrum is better for wind tunnel modelling. IEC [19]suggests the Mann spectrum (modified von Kármán type spectrum) and the Kaimal spectrum, while DNV [6] suggests the Kaimal spectrum, which was chosen in this paper.

Several characteristics and simplification introduced by the Kaimal spectrum are given here. The power spectrum of turbulence can be modified by the landscape: if the inhomogeneity of the surface is high, the turbulence intensity increases. Inhomogeneous terrain typically generates eddies of the same length scale as that of the inhomogeneity itself, increasing power in the corresponding frequency range. For offshore wind turbine applications this effect is less relevant for winds blowing onshore from open sea, but can have important effects for offshore winds blowing from the land [25]. Another important aspect is whether the stratification is stable, unstable or neutral. Neutral conditions rarely occur, but near-neutral conditions are typical for medium and high wind speeds, which is most important for fatigue damage calculation, and it is assumed for the Kaimal spectrum used here. Further details can be found in [24]

It is to be noted that the several limitations pointed out here are referring to the use of the Kaimal spectrum for modelling. However, the methodology described here can be used with any power spectrum, the use of site specific spectra is encouraged whenever available [6]. The PSD function can be determined

from site measurements by Discrete Fourier Transform (DFT) [4], [5]. Such data are typically available for offshore wind farm developments as they are required for the assessment of expected energy production as well.

The theoretical Kaimal spectrum for a fixed reference point in space in neutral stratification of the atmosphere $S_{uu}(f)$ as suggested by DNV [6][18] can be written as:

$$S_{uu}(f) = \frac{\sigma_U^2 \left(\frac{4L_k}{\overline{U}}\right)}{\left(1 + \frac{6fL_k}{\overline{U}}\right)^{\frac{5}{3}}} \tag{2}$$

where L_k is the integral length scale (formula available in the DNV code), f is frequency, $\overline{U}$ is the mean wind speed (from site measurements), and σ_U is the standard deviation of wind speed (from measurements or calculated using Equation 1 and turbulence intensity values from standards IEC 61400-1 [19] and IEC 61400-3 [26]). The turbulence intensity is generally lower offshore than onshore considering reports [25]. The turbulence intensity increases in the wake of the wind turbines, but this effect is beyond the scope of this paper.

Figure 3 shows a comprehensive wind spectrum following van der Hoven [27] where both long term variations of wind speed and turbulence effects are plotted. Van der Hoven observed a significant 4 day synoptic peak and in some cases a small diurnal peak in the spectrum of the horizontal wind speed. The Kaimal spectrum describes wind turbulence on a short time scale (shown by a dotted line in Figure 3) i.e. represents only the high frequency end of the spectrum omitting the diurnal and synoptic peaks. Therefore, even though the Kaimal spectrum can be calculated for arbitrarily low frequency, its validity is limited to the high frequency variations. The lowest frequency considered in this work corresponds to the time interval of 10 minutes, because the mean is taken over 10 minutes ($T = 600\ [s] \rightarrow f = 1/600[Hz] \approx 0.0017[Hz]$). The representation of the Kaimal spectrum shown in Figure 4(a) is more convenient for the present discussion, in aerodynamics and wind engineering applications often the normalised spectrum on logarithmic scales is used (see Figure 4(b)).

Several important aspects of wind spectra should be considered. One important property of the Kaimal spectrum is that it describes turbulence at one point in space. To properly represent the turbulent flow field on the large rotor area (typically in the order of magnitude of 10,000 [m^2]), covariance spectra need to be employed.

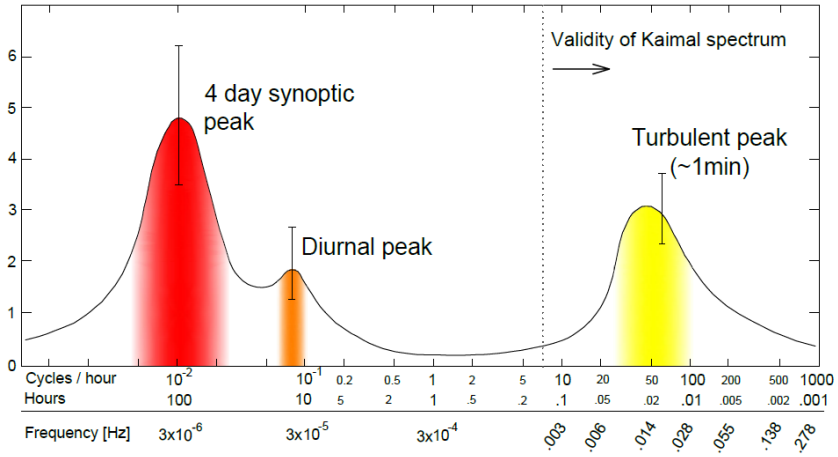

Figure 3 – Van der Hoven wind spectrum [27] *and the validity of the Kaimal spectrum*

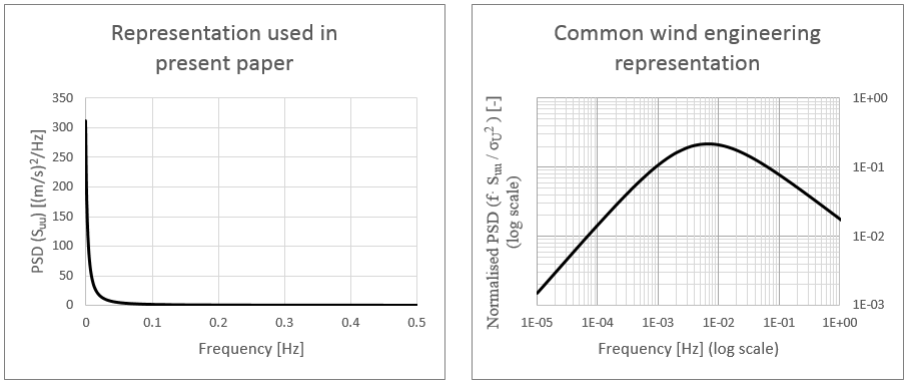

Figure 4 – Two representations of the Kaimal spectrum. (a) Representation used in present paper. (b) Normalised, representation common in aerodynamics and wind engineering applications (on logarithmic scale).

A small local gust (say of 20m diameter) passing through the rotor has small or no effect on distant parts of the rotor area, while a large gust (say of 300m diameter) has similar effects on the whole rotor. Referring to Figure 5, the wind speeds of the points A and B are closely related and they show a high coherence, while a distant point, such as C in the figure, has a low coherence with either A or B. In other words, low frequency variations effect a larger area of the rotor than high frequency variations.

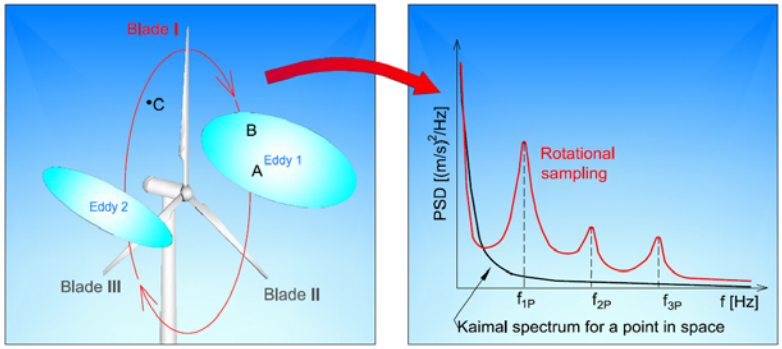

Figure 5 – Coherence: Coherence between points A and B is high, while between C and either A or B the coherence is small. Rotational sampling: the PSD of the wind speed "seen" by Blade 1 while rotating differs from the Kaimal spectrum for a point in space. The graph is a schematic representation of the PSD of rotational sampling.

It should also be noted that through their rotary motion the blades experience a different spectrum from the Kaimal spectrum for a point in space. The blade will pass through any given eddy once in every revolution. In Figure 6, Blade I for example passes through Eddy 1 and Eddy 2 once in each revolution. Therefore, when rotational sampling is considered, that is, the wind speed "seen" by the rotating blade is sampled, the PSD will show peaks at the rotational frequency f_{1P} and at higher harmonics $(f_{2P} = 2f_{1P}, f_{3P} = 3f_{1P})$. This effect is a more important for blade load analysis, usually only higher harmonics are transferred to the hub as typically all blades pass through the same eddies. More information about spatial coherence and rotational sampling is available in [28]and [29].

2.2. Wind load spectrum.

The spectral density of the wind speed is represented by the Kaimal spectrum shown in Equation 2. Since the thrust force on the rotor is proportional to the square of the wind speed, a moment spectrum can be determined from the PSD of the wind speed. The thrust force on the rotor at a given wind speed is given in Equation 3.

$$Th = \frac{1}{2}\rho_a A_R C_T U^2 \qquad U = \overline{U} + u \qquad (3)$$

where Th is the thrust force, ρ_a is the density of air, U is the wind speed, A_R is the rotor swept area and C_T is the thrust coefficient which depends on the mean wind speed. Using quasi-steady assumptions, the wind speed can be considered as a mean wind speed $\overline{U}$ and a small fluctuating component u. With these, the thrust force can be written as the sum of a static wind load Th_{stat} and a fluctuating, dynamic wind load Th_{dyn}. In Equation 4 the second order terms of the small wind speed variation u are neglected.

$$Th = \frac{1}{2}\rho_a A_R C_T(\overline{U})(\overline{U}^2 + 2\overline{U}u + u^2) \approx \frac{1}{2}\rho_a A_R C_T(\overline{U})\overline{U}^2 + \rho_a A_R C_T(\overline{U})\overline{U}u = \\ = Th_{stat} + Th_{dyn} \tag{4}$$

The spectral density of the turbulent thrust force on the rotor $S_{FF,wind}(f)$ can be written as:

$$S_{FF,wind}(f) = \rho_a^2 \frac{D^4\pi^2}{16} C_T^2 \overline{U}^2 \sigma_U^2 \tilde{S}_{uu}(f) = \rho_a^2 \frac{D^4\pi^2}{16} C_T^2 \overline{U}^4 I^2 \tilde{S}_{uu}(f) \qquad \tilde{S}_{uu}(f) = \frac{S_{uu}(f)}{\sigma_U^2} \tag{5}$$

where D is the diameter of the rotor, $S_{uu}(f)$ is the Kaimal spectrum, $\tilde{S}_{uu}(f)$ is the Normalised Kaimal Spectrum, ρ_a is the density of air, C_T is the thrust coefficient, I is the turbulence intensity (value taken from standards), σ_U is the standard deviation of wind speed. The thrust coefficient of a wind turbine rotor can be calculated by the Blade Element Momentum theory [15] and other more complex methods. However, as it is demonstrated in [30], a very simple approximation provides conservative and relatively accurate results for most offshore wind turbines in the important wind speed range:

$$C_T = \frac{3.5 \cdot (2\overline{U} - 3.5)}{\overline{U}^2} \approx \frac{7}{\overline{U}} \tag{6}$$

This approximation is also implemented in the IEC 61400-1 standard in Amendment 1, 3rd Edition [31]. With the above given formulae the fore-aft bending moment at the mudline is simply given by:

$$M_{wind} = Th(H + MSL) \tag{7}$$

where H is the hub height above mean sea level and MSL is the mean sea depth (see Figure 6). Similarly, the load can be reduced to any other cross section, such as the transition piece (TP). The mudline moment spectrum associated with wind speed fluctuations can be expressed as:

$$S_{MM,wind}(f) = \rho_a^2 \frac{D^4\pi^2}{16} [C_T(\overline{U})]^2 \overline{U}^4 I^2 (H + MSL)^2 \tilde{S}_{uu}(f) \tag{8}$$

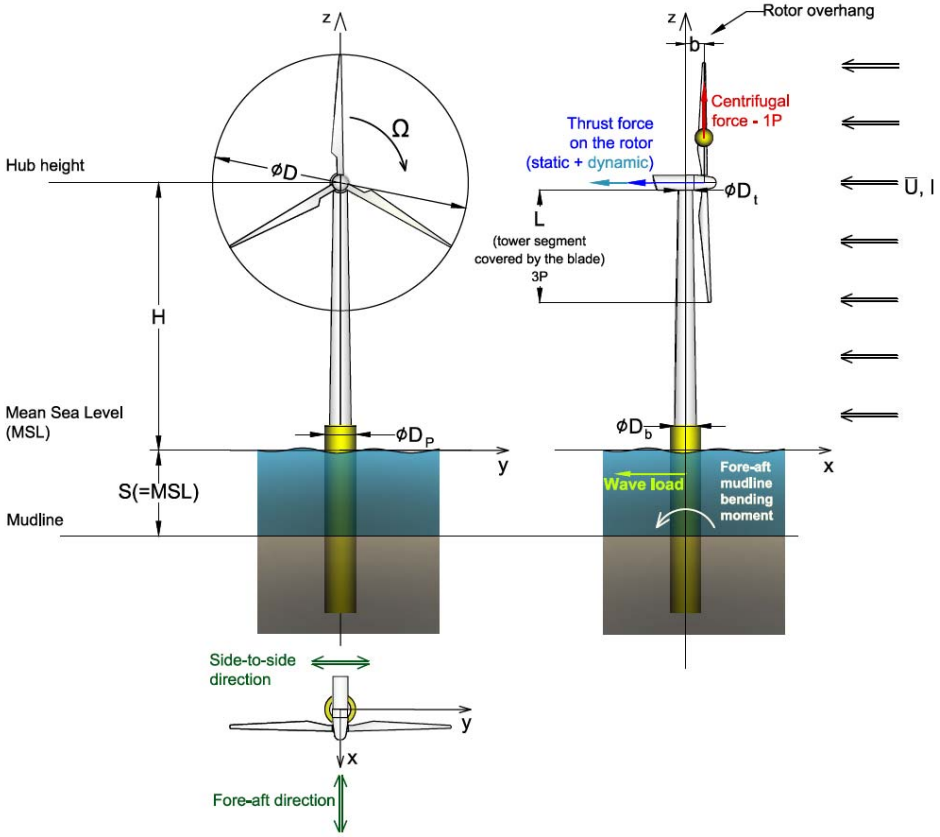

Figure 6 – Definition of the geometry, axes, loads and directions of the Offshore Wind Turbine Structure

A few points may be noted:

1. The bending moment spectrum caused by wind turbulence is explicitly or implicitly dependent on the parameters shown in Equation 9 (see nomenclature at the beginning of the paper).

$$S_{MM,wind} = S_{MM,wind}(f, D, H, MSL, \overline{U}, I, \rho_a, L_k, C_T) \tag{9}$$

2. Using practical assumptions about the turbine and the site, several parameters can be considered constant. Such parameters are the rotor diameter, the hub height above sea level and the mean sea depth (neglecting tides and surges), the turbulence intensity (aiming for an upper bound estimate, its dependence on the wind speed, wind direction, sea state and atmospheric conditions can be neglected), the density of air, and the integral length scale. Also using the assumption in Equation 6 the following remains:

$$S_{MM,wind} = S_{MM,wind}(f, \overline{U}) \tag{10}$$

3. It is important to note that the mudline moment spectrum is dependent on the 10 minutes mean wind speed, because turbulence intensity varies with wind speed. The dynamic forcing is proportional to $\overline{U}$.
4. The coherence between points in the rotor area can be modelled by an aerodynamic admittance function (AAF); denoted by $\chi(f)$. The AAF assigns a value to each frequency depending on how much the variations in wind speed with given frequency are admitted in the fluctuating wind force. Using $\chi(f)$ the moment spectrum is written as:

$$S_{MM,wind}(f) = \rho_a \frac{D^4 \pi^2}{16} C_T^2 \overline{U}^4 I^2 (H + MSL)^2 \tilde{S}_{uu}(f) \chi^2(f) \tag{11}$$

The maximum value of AAF $\chi(f)$ is 1 and has lower values at higher frequencies because small eddies contribute less to the total force. Taking the constant AAF value of 1 provides an upper estimate for the

mudline moment spectrum, although it significantly overestimates the load caused by high frequency fluctuations.

2.3 Wave loading.

The wind blowing over the sea generates wind waves because of the increased pressure on the free surface of water. Firstly small waves are produced with high frequency and low wave height, and the energy is gradually transferred towards the higher amplitude waves with lower frequency and longer wavelength. The developing sea state depends on many factors, including but not limited to the water depth, the shape of the sea bottom, the mean wind speed and the fetch. The latter is the typical leeward distance to shore considering the prevailing wind direction. The dependence on the water depth is apparent from the dispersion relation [6], [32]:

$$\omega^2 = gk\tanh(kS) \tag{12}$$

where $\omega[rad/s]$ is the angular frequency, $k = 2\pi/\lambda[1/m]$ is the wave number with $\lambda[m]$ being the wavelength, and $S[m]$ is the mean sea depth.

A certain sea state consists of a large number of waves with various frequencies and wavelengths. The importance of each frequency is characterised by the power associated with it, which is represented by the PSD function. The PSD can be produced from site measurements of the wave height using DFT, or alternatively the JONSWAP (Joint North Sea Wave Project) spectrum $S_{ww}(f)$ suggested by DNV [16] can be used:

$$S_{ww}(f) = \frac{\alpha g^2}{(2\pi)^4 f^5} e^{-\frac{5}{4}\left(\frac{f}{f_p}\right)^4} \gamma^r \qquad \gamma = 3.3$$

$$r = e^{-\frac{(f-f_p)^2}{2\sigma^2 f_p^2}} \qquad \alpha = 0.076\left(\frac{\bar{U}_{10}^2}{Fg}\right)^{0.22} \qquad f_p = \frac{22}{2\pi}\left(\frac{g^2}{\bar{U}_{10}F}\right)^{\frac{1}{3}} \qquad \sigma = \begin{cases} 0.07 & f \le f_p \\ 0.09 & f > f_p \end{cases} \tag{13}$$

where f is frequency, α is the intensity of the spectrum, F is the fetch, f_p is the peak frequency, γ is the peak enhancement factor, g is the gravitational constant, $\bar{U}_{10}$ is the mean wind speed at 10 metres height above sea level.

It should be noted that the JONSWAP spectrum (as well as the Pierson-Moskowitz spectrum) represents the frequency content of a sea state developed in a constant wind speed condition after a sufficiently long time. The Pierson-Moskowitz spectrum [33] assumes a fully developed sea, and that the process transferring energy from high to low frequency waves and the wave-wave interaction have reached a steady state, the waves are in equilibrium with the wind. This assumption requires a sufficiently long fetch (about five thousand wave lengths), and that the constant wind velocity has maintained for sufficiently long time (about ten thousand wave periods) [32]. The JONSWAP spectrum takes the fetch into account and thus considers a developing sea. It can be seen from Equation 13 that the peak frequency of the spectrum depends on the mean wind speed and the fetch. The longer the fetch, the more developed the sea is and the more energy is in the low frequency waves.

The fetch can greatly differ for offshore wind farms on different coasts. Figure 7 shows a relatively sheltered sea location where the sea is typically not fully developed. A schematic wind rose is placed at the location of the turbine. A method to estimate the fetch is to take the average of the distances to leeward shores (e.g. F_S, F_{SSW}, F_{SW} etc), adding weights to the distances based on the significance of the direction. For example, in Figure 7 the prevailing wind is blowing from south-southwest (SSW) and southwest (SW), therefore the weights of the distances F_{SSW}, F_{SW} will be the highest in the weighted average of the distances F_i. Figure 8 shows the significant wave height (Figure 8(a)) and the peak wave period (Figure 8(b)), as functions of the mean wind speed. Curves (1) to (5) represent the JONSWAP spectrum for increasing fetch, curve (6) shows the Pierson-Moskowitz spectrum. (See Remark 4 at the end of Section 2.2 for addition information about JONSWAP parameters.) Curves (1) to (5) in Figure 9(a) show the JONSWAP spectrum for increasing mean wind speeds keeping the fetch constant at 60[km], while curves (1) to (5) in Figure 9(b) presents the JONSWAP spectrum for increasing fetch, keeping the mean wind speed constant at 10 [m/s].

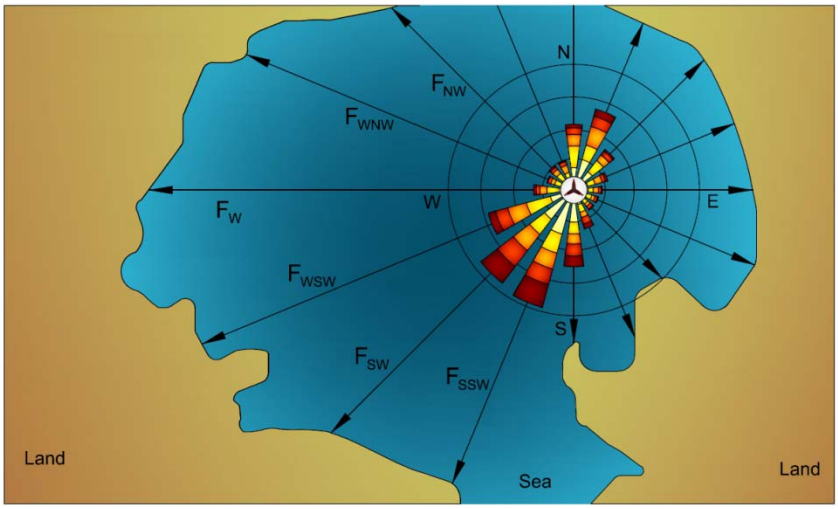

Figure 7 – Estimation of the fetch F_i where i represents the directions of the 16-point compass rose (e.g. S for south, SW for southwest, SSW for south-southwest, etc).

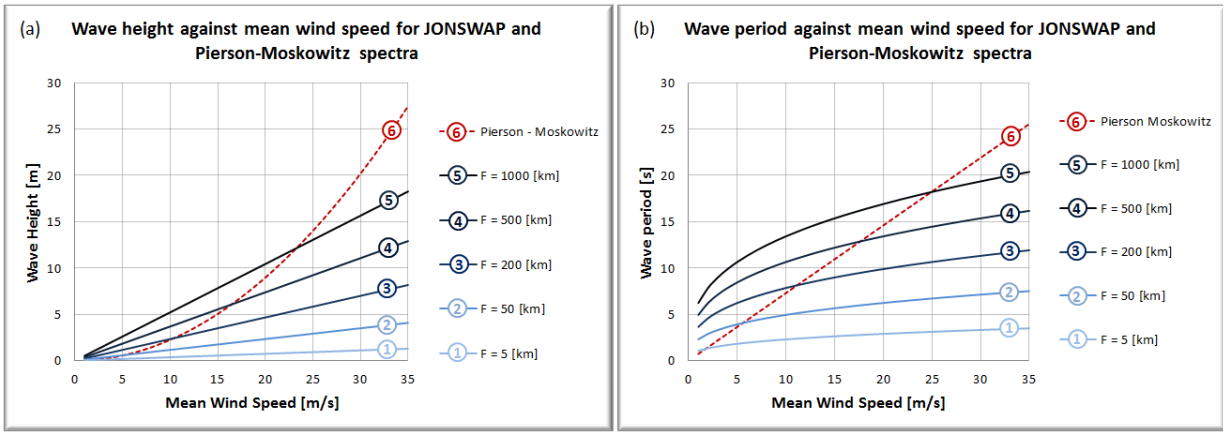

Figure 8 – Wave height and wave period as a function of mean wind speed for the Pierson-Moskowitz spectrum and for several values of fetch using the JONSWAP spectrum. Walney site with water depth of 21.5m

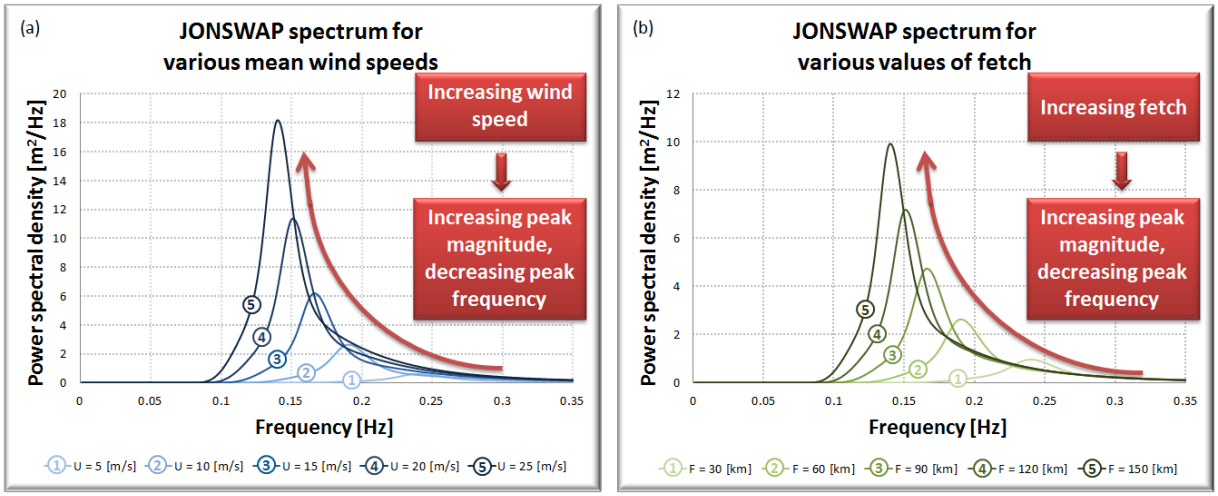

Figure 9 – (a) JONSWAP spectrum for several values of the mean wind speed with a constant fetch of 60km. (b) JONSWAP spectrum for several values of fetch F keeping the wind speed constant at 10m/s.

2.4 Wave load spectrum.

The DNV code suggests the JONSWAP spectrum for offshore wind turbine applications (given in Equation 16), and it is dependent on the mean wind speed and the fetch. The JONSWAP spectrum is a spectral density of wave heights and has units of [m^2/Hz]. The wave height spectrum needs to be transformed to a mudline moment spectrum. To determine the wave loading, simple linear waves are assumed, which is a rough estimation. Higher order theories like Stokes waves [34] or Dean's Stream Function Theory [35] would provide more accurate results, especially in shallow waters [6], [18]. However, the linear theory allows for simpler load calculation and its usage can be justified. The study in [36] estimates a fatigue damage increase of 7.5% on the foundation with second order wave models using a Wöhler exponent of 5. In another paper Veldkamp and van der Tempel [37] found that the fatigue damage increase using more sophisticated models of wave kinematics is about 5-10% and they concluded it is "on the threshold of significance." The force exerted by the waves on the support structure is estimated by Morison's equation [38]:

$$dF_T(z,t) = dF_D(z,t) + dF_I(z,t) = \frac{1}{2}\rho_w D_P C_D u(z,t)|u(z,t)| + C_m \rho_w A_P \dot{u}(z,t) \tag{14}$$

where dF_T, dF_D and dF_I are the total wave force, the drag force and the inertia force per length, respectively; C_D is the drag coefficient of the support structure with suggested values between 0.7-1.2 [6]; $C_m = 1 + C_a$ is the inertia coefficient with suggested values between 1.5-2 [6]; C_a is the added mass coefficient, ρ_w is the density of water, D_P is the diameter of the monopile/substructure, $A_P = D_P^2\pi/4$ is the cross sectional area of the pile (more precisely, the area of the outer circle). The total force F_T and total mudline moment M_T can be expressed in integral form:

$$\begin{aligned} F_T(t) &= \int_{-S}^{\eta} dF_D dz + \int_{-S}^{\eta} dF_I dz \\ M_T(t) &= \int_{-S}^{\eta} dF_D(S+z)dz + \int_{-S}^{\eta} dF_I(S+z)dz = \end{aligned} \tag{15}$$

where $F_T(t)$ and $M_T(t)$ are functions of time t. z is the vertical coordinate along the support structure with its zero at Mean Sea Level (MSL), η is the surface elevation and S is the mean sea depth. For definitions see Figure 10.

It is to be noted that Morison's equation is limited to slender piles. As argued in [39] Morison's equation ignores sea surface effects of water falling and rising around the column, and also three dimensional effects and diffraction. Because of these, Morison's method is not suitable for large diameter sections or complex geometries, such as gravity base structures, and its validity has to be assessed for very large diameter substructures.

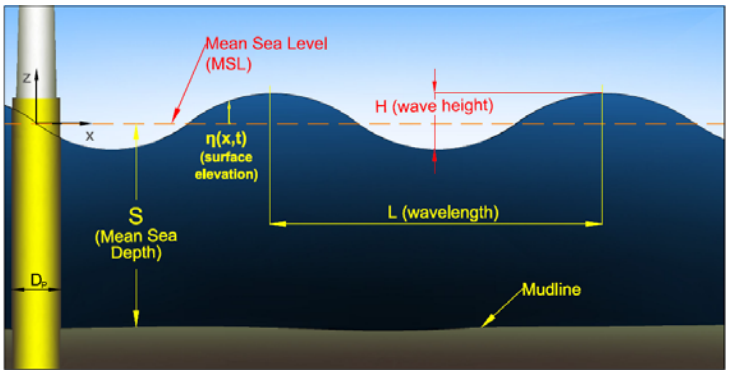

Figure 10 – Definition of wave parameters.

The velocity and acceleration profiles are required to compute the wave loads. These are determined using first order Airy waves and are taken at the pile of the substructure ($x = 0$), The velocity profile $u(z,t)$ and the acceleration profile $\dot{u}(z,t)$ as functions of depth and time are given by Equation 16

$$u(z,t) = \frac{\pi H_{1/3}\cosh(k(S+z))}{T\sinh(kS)}\cos\left(\frac{2\pi t}{T}\right) \qquad \dot{u}(z,t) = \frac{2\pi^2 H_{1/3}\cosh(k(S+z))}{T^2\sinh(kS)}\sin\left(-\frac{2\pi t}{T}\right) \tag{16}$$

where $k = 2\pi/\lambda$ is the wave number, λ is the wave length of the ocean waves, z is the vertical coordinate, t is time, $H_{1/3}$ is the significant wave height (average height of the highest one third of the waves), T is the wave period. The wave number can be determined from the dispersion relation (see Equation 12), he wave period T and the significant wave height $H_{1/3}$ are calculated from the JONSWAP spectrum. The significant wave height is calculated as shown in Equation 17 [6], [32]).

$$H_{1/3} = 4\sqrt{\langle\zeta^2\rangle} \qquad \langle\zeta^2\rangle = \int_0^\infty S_{ww}(f)df = 1.67\cdot 10^{-7}\frac{U_{10}^2}{g}F \tag{17}$$

The peak frequency is determined from Equation 13; from that the peak wave period is written in Equation 18.

$$T_p = \frac{1}{f_p} \tag{18}$$

Using the calculated time period and significant wave height, an equivalent first order Airy wave can be considered and the wave force on the substructure calculated as a function of time. To determine the amplitude of the periodic moment on the structure, the maximum of the total load and the time instant of this maximum has to be determined. Since the velocity is a cosine and the acceleration is a sine function of time, the drag force and the inertia force have 90° phase difference. Figure 11(a) shows the general shape of the wave forces on the substructure. In present case the expression for the force can be simplified by examining the dominant component of the force. The Kreulegan-Carpenter number is a good measure of the ratio of the drag and inertia forces:

$$K_C = \frac{u_{max}T_p}{D_P} = \frac{\pi H_{1/3}}{D_P}\coth(kS) \tag{19}$$

where u_{max} is the maximum of the horizontal component of the periodic water particle velocity, T_p is the wave period, D_P is the diameter of the pile, k is the wave number and S is the mean sea depth. If $K_C < 5$ the load is said to be inertia dominated, and the drag force may be neglected. For a wind turbine at the Walney 1 site in typical environmental conditions $K_C \approx 0.59$ and the load is heavily inertia dominated as shown in Figure 11(b).

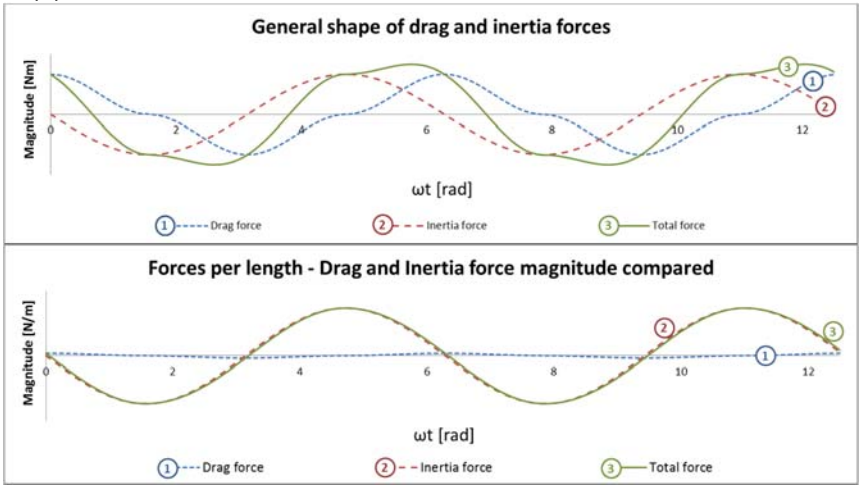

Figure 11 – Forces from waves on the structure. General shape of forces as a function of time and magnitudes compared for an actual wind turbine (Siemens SWT-3.6-107 Walney, 21.5m water depth, average wind and waves).

Therefore the maximum of the total force approximately coincides with the maximum of the inertia force, which is found when the acceleration is maximum. The amplitude of the mudline moment becomes:

$$M_{T,max} = M_{I,max} = \int_{-S}^{\eta} dF_{I,max}(S+z)dz$$
$$M_{T,max} = C_m \rho_w \frac{D_P^2 \pi^3}{2} \frac{H_{1/3}}{T^2 \sinh(kS)} \int_{-S}^{\eta} \cosh\big(k(S+z)\big)(S+z)dz \quad (20)$$

The wave number k is connected to the wave frequency f by the dispersion relation (see Equation 12) and the wave period T is connected to the wave frequency f by Equation 18. The upper limit of the integral on the right hand side is the surface elevation; its value is zero at the instants ϑ_n of the maxima of the inertia force, that is, $\eta(\vartheta_n) = 0$. The integration is carried out in Equation 21.

$$Q(k,S) = \int_{-S}^{0} \cosh\big(k(S+z)\big)(S+z)dx = \left(\frac{S}{2k} - \frac{1}{2k^2}\right)e^{kS} - \left(\frac{S}{2k} + \frac{1}{2k^2}\right)e^{-kS} + \frac{1}{k^2} \quad (21)$$

Using these the power spectral density of the mudline bending moment can be written (Equation 22).

$$S_{MM,waves}(f) = C_m^2 \rho_w^2 \frac{D_P^4 \pi^6}{4} \frac{f^4}{\sinh^2(kS)} \left[\left(\frac{S}{2k} - \frac{1}{2k^2}\right)e^{kS} - \left(\frac{S}{2k} + \frac{1}{2k^2}\right)e^{-kS} + \frac{1}{k^2}\right]^2 S_{ww}(f) \quad (22)$$

Remarks:

1. The mudline moment spectrum of the wave loads is explicitly or implicitly dependent on the parameters shown in Equation 23 (see Nomenclature at the beginning of the paper).

$$S_{MM,waves}(f) = S_{MM,waves}(f, C_m, \rho_w, D_P, k, S, \overline{U}, F) \quad (23)$$

2. Establishing the mudline moment spectrum for a given site with a given wind turbine and support structure and using practical approximations, the inertia coefficient, the water density, the diameter of the pile, the water depth (if the tidal and surge variations are neglected) and the fetch can be considered constant and Equation 23 reduces to:

$$S_{MM,waves} = S_{MM,waves}(f, k, \overline{U}) \quad (24)$$

3. In sufficiently deep ($S > \lambda\backslash 2$) or sufficiently shallow ($S < \lambda/10$) waters approximations may be used for the dispersion relation:

   Deep water: $\omega^2 = gk \rightarrow k = 4\pi^2 f^2/gS > \lambda/2$

   Shallow water: $\omega^2 = gk^2 S \rightarrow k = 2\pi f/(gS) \qquad S < \lambda/10$

   Expressing the wave number with the frequency, Equation 24 can be further reduced to:

$$S_{MM,waves}(f) = S_{MM,waves}(f, \overline{U}) \quad (25)$$

4. The two main parameters in the representation of the JONSWAP spectrum as expressed in Equation 13 are the mean wind speed $\overline{U}_{10}$ and the fetch F. It should be noted that such direct relationship between wind speed and wave height cannot always be established, for example because of the presence of swell waves (i.e. waves generated by storms far away from the wind turbine). Therefore, it is often more practical to use the significant wave height $H_{1/3}$ and the time period of waves T_p as main parameters. They are also more practical in some cases because they are observable and can be measured. Such representation is shown in the DNV-RP-205 code for Environmental Conditions and Environmental Loads [18].

$$S_J(f) = 2\pi \cdot A_\gamma H_{1/3}^2 T_p^{-4} f^{-5} e^{-1.25\, T_p^4 f^{-4}} \cdot \gamma^r$$
$$r = e^{-\frac{T_p^2}{2\sigma}(f - f_p)^2} \qquad \sigma = \begin{cases} 0.07 & f \le 1/T_p \\ 0.09 & f > 1/T_P \end{cases} \qquad A_\gamma = 1 - 0.287 \ln(\gamma) \quad (26)$$

   where $S_J(f)$ is the JONSWAP spectrum, f is the frequency of waves, A_γ is a normalizing factor, $H_{1/3}$ is the significant wave height, T_p is the peak wave period and γ is the peak enhancement factor.

2.5 1P loading

The wind turbine is subject to cyclic loading with the rotational frequency and the source of this load is mainly the rotor mass imbalance and aerodynamic imbalance (due to differences in the pitch of individual blades). The amplitude of this forcing depends on the extent of the imbalances, and a typical value is used here based on the literature (see [20], [21]). A simple method is shown to estimate the fore-aft bending moment at the mudline caused by the mass imbalance, however, the calculation of the effect of blade pitch misalignment requires more input information and more sophisticated methods. The mass imbalance can be modelled as an added lumped mass on the rotor at θ azimuthal angle from Blade I. and at R distance from the centre of the hub as shown in Figure 12. Here the imbalance is assumed to be on Blade I ($\theta = 0$).

$$I_m = mR \tag{27}$$

where I_m is the mass imbalance with units of $[\mathrm{kg} \cdot \mathrm{m}]$, m is a lumped mass and R is the radial distance from the centre of the hub along Blade I. The centrifugal force at any time can be calculated from the centrifugal acceleration $a = R\Omega^2$ with Ω being the angular frequency and $f = \Omega/(2\pi)$ the frequency of rotation. The lever arm of the centrifugal force F_{cf} is called the rotor overhang b (see Figure 13), with which the bending moment is expressed:

$$F_{cf} = ma = mR\Omega^2 = I_m\Omega^2 = 4\pi^2 I_m f^2 \qquad M_{1P} = 4\pi^2 b I_m f^2 \tag{28}$$

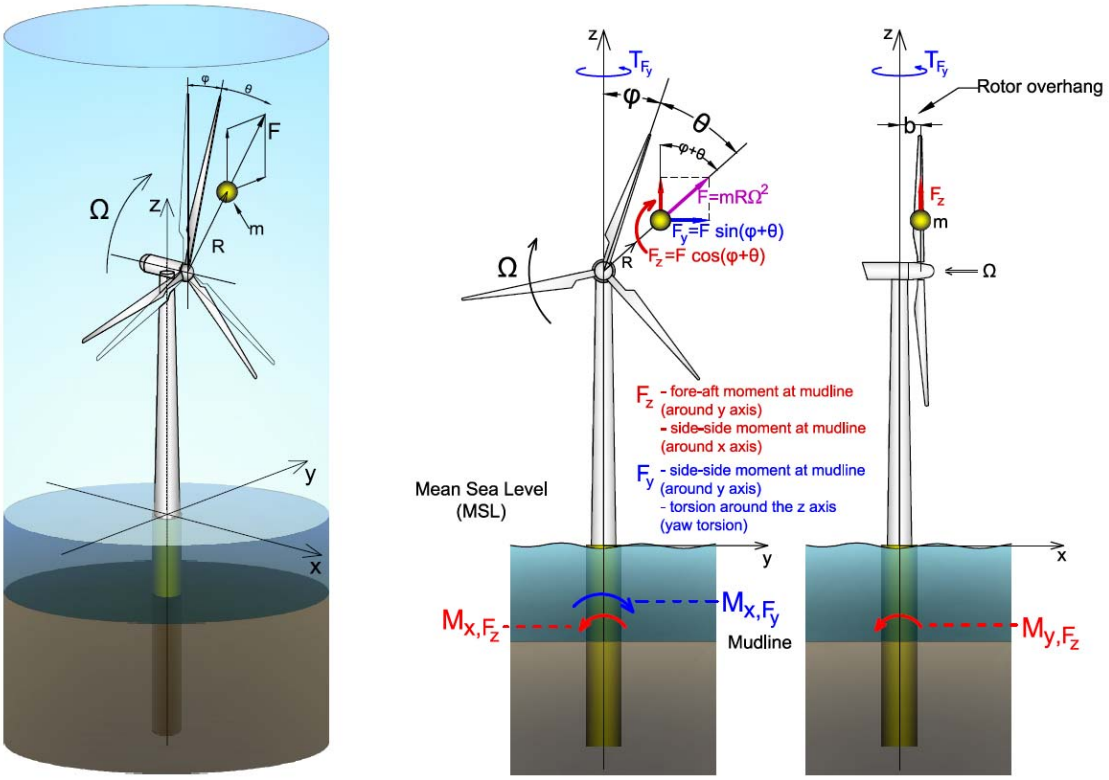

Figure 13 –Model of the mass imbalance and loads exerted during operation. The fore-aft mudline bending moment caused by the wind load and waves (assumed collinear) is M_{y,F_z}.

It is to be noted here that the centrifugal force also produces torsion in the tower (around the x axis), as well as moments in side-to-side direction (around the z axis) as shown in Figure 13. The bending moment in the side-side direction caused by the centrifugal force is much higher than the fore-aft moment because the arm of the force is $H + MSL$ instead of b. The effect of the gravity force acting on the mass imbalance is considered negligible.

The spectral analysis of a load that is essentially a sinusoidal function of a certain frequency gives a Dirac-Delta function. This is a function defined as $\delta(f - f_{1P}) = 0$ for all values of f except for $f = f_{1P}$ where

$\delta(f - f_{1P}) \neq 0$ (with f_{1P} being the frequency of the wind turbine's rotation.) The magnitude of this function at $f = f_{1P}$ is strictly undefined. However, the conditions in Equation 29 apply.

$$\int_{-\infty}^{\infty} \delta(f - f_{1P})df = 1$$
$$\int_{-\infty}^{\infty} M_{1P}^2(f)\delta(f - f_{1P})df = M_{1P}^2(f_{1P}) \quad (29)$$

This means that the condition that the integral of the spectral density function has to give the variance of the signal, that is, the square of the amplitude of the load, is satisfied. Thus the spectrum of the 1P loading is given in Equation 30.

$$S_{MM,1P} = M_{1P}^2(f)\delta(f - f_{1P}) \quad (30)$$

For constant speed wind turbines f_r is constant, however, for the more common variable speed wind turbines which operate at different rotational speeds based on the wind speed, the frequency of the rotation depends on the mean wind speed at hub height $f_{1P} = f_{1P}(\overline{U})$. A higher frequency also means a higher value of the integral under the Dirac-Delta curve, that is

$$\overline{U}_1 < \overline{U}_2 \rightarrow f_1 < f_2 \rightarrow \int_{-\infty}^{\infty} M_{1P}^2(f)\delta(f - f_1)df \leq \int_{-\infty}^{\infty} M_{1P}^2(f)\delta(f - f_2)df \quad (31)$$

2.6 Blade passage (3P).

The wind produces drag force on the tower, which can be considered constant at a given mean wind speed ignoring buffeting and vortex shedding on the tower and also without the effect of the rotating. When a blade is passing in front of the tower it disturbs the flow downwind and decreases the load on the tower. The frequency of this load loss is three times the rotational frequency of the turbine 3P (2P in case of 2-bladed designs). In this paper its magnitude is estimated by a simple geometric consideration: the upper part of the face area of the tower is partly covered by the blade when the blade is in a downward pointing position ($\varphi = \pi$). The drag force on the covered part of the tower is taken to be zero; the blade causes a load loss on the tower. When the blade is in the downward direction it covers the tower from $z = H - L$ to $z = H$. The total moment of drag force on this upper section without the effect of blade passage:

$$M_{drag} = \int_{H-L}^{H} \frac{1}{2}\rho_a C_D D_T(z)U^2(z)(z + S)dx \qquad U(z) = \overline{U}\left(\frac{z}{H}\right)^{\beta} \quad (32)$$

where H is the hub height from mean sea level, L is the length of the blades, ρ_a is the density of air, C_D is the drag coefficient, $D(z)$ is the diameter of the tower at z (assuming the diameter linearly decreases between the bottom and top diameters), z is the vertical coordinate (zero at mean sea level), S is the mean sea depth and $U(z)$ is the power law velocity profile using the exponential wind profile with $\beta = 1/7 \approx 0.143$. If the ratio of the face area of the blade and the area of the top part of the tower (see Figure 6) is R_A, then the 3P moment amplitude can be written:

$$M_{3P} = R_A M_{drag} \quad (33)$$

Similarly to the 1P loading, the frequency of this loading is constant at a given rotational speed of the turbine, therefore its power spectrum is a Dirac-delta function. The integral under the curve equals to the square of the 3P moment, with the amplitude of the Dirac-delta undefined. The integral is not directly dependent on the frequency of rotation, however, it depends on the mean wind speed, and the mean wind speed and the rotational speed of the turbine are connected through turbine characteristics.

$$\int_{-\infty}^{\infty} \delta(f - f_{3P})df = 1$$
$$\int_{-\infty}^{\infty} M_{3P}^2(f)\delta(f - f_{3P})df = M_{3P}^2(f_{3P}) \quad (34)$$
$$S_{MM,3P} = M_{1P}^2(f)\delta(f - f_{1P})$$

2.7 Dynamic Amplification

As mentioned above, close to the natural frequency of the structure dynamic amplification increases the fatigue damage suffered by the structure. The magnitude of the response of the structure increases by the Dynamic Amplification Factor (DAF), which depends on the modal damping of the system. The main contributors to the damping of tower vibrations of an OWT are material/structural, soil, hydrodynamic and most importantly aerodynamic damping. The value of structural damping varies in the literature. One finds as low values as 0.3% suggested in [15] and 0.5% in [25], intermediate value of "less than 1%" in [40] and about 1% in [41], the range 0.5-1.5% in [42], and higher values of 2% in [43] and [44]. For the soil damping ratio the value of about 0.4-0.7% was found in [45], 0.6-0.8% was estimated in [46], about 1.5% in [47]. The hydrodynamic damping consists of two main effects, viscous damping (dissipation due to drag) and wave radiation [46]. The study in [45] considers the viscous damping negligible and uses the wave radiation damping value of about 0.1%. Similarly, [25] found the hydrodynamic damping negligible due to very low velocities and accelerations of the structure close to seabed. The aerodynamic damping of depends on the wind speed and differs for the along-wind (fore-aft vibrations) and cross-wind (side-to-side vibrations) directions. In the along-wind direction (fore-aft vibration) one finds values in the range of 4-7% in the literature [25], [41], [43], and in the cross-wind direction low values are reported, e.g. 0.1% was found in [48] and about 0.1-0.25% in [46].

A significant difference between estimated and measured damping ratios was found in [43]. The HAWC software predicted total damping values of 5.5% and 0.6% in the along-wind and cross-wind directions, respectively, while the measured values were about 11-14% in the along-wind and 3.2-7.9% for the cross-wind directions, with the cross-wind damping decreasing at higher wind speeds. This may suggest that actual values of damping are higher than those estimated in literature. However, to stay on the conservative side, in this study a total damping ratio of 5% is assumed in the fore-aft direction, most of which is the contribution from aerodynamic damping, and in the side-to-side direction a low damping ratio of 0.5% is used.

The DAF is estimated by the formula given in the DNV code [6]

$$DAF = \frac{1}{\sqrt{(1-\beta^2)^2+(2\xi\beta)^2}} \qquad \beta = \frac{f}{f_0}\left(= \frac{excitation\ frequency}{natural\ frequency}\right) \qquad \xi = damping\ ratio$$

The PSD magnitudes need to be multiplied by the square of the DAF to include dynamic amplification.

3. Application of the method for an industrial wind turbine

The method presented above is applied here for an actual Siemens industrial wind turbine of 3.6MW rated power at the Walney 1 wind farm site. The necessary turbine and site information are available in the Siemens brochure [49], website of DONG Energy (the developer of the wind farm) [50], website of the Lindoe Offshore Renewables Center [51], lorc.dk. All necessary information is presented in Table 1.

In this section the mudline moment spectra are derived for each loading and some load values are estimated for several typical operational conditions of the particular turbine. Dynamic amplification is taken into account.

3.1 Walney 1 Wind Farm Site

The Walney site is located 14km off the coast of Walney Island in the Irish Sea (UK). The first phase (Walney 1) of the wind farm contains 51 Siemens SWT-3.6-107 type wind turbines of 3.6MW rated power. The average wind speed at the site is 9m/s, the dominant wind direction is West/South-West. This location in the Irish Sea is relatively sheltered as the shores are relatively close in most directions. The average fetch is estimated at 60km and this value is used to calculate the JONSWAP spectrum. The significant wave heights are limited at the site and the highest waves are in the range of a few metres. The water depth ranges between 19-23m at the site and in the calculations an average value of 21.5m is used. A conservative upper bound estimate of 16% is assumed for the site turbulence intensity (IEC high turbulence site [26]).

The OWT's cut-in wind speed is 4m/s and its cut-out speed is 25m/s, the rated wind speed is 13-14m/s. The turbines are pitch regulated variable speed turbines, the rotational speed ranges between 5-13rpm. The OWTs have a rotor diameter of 107m, the hub height is 83.5m above mean sea level. A tapered tubular tower is assumed with linearly varying diameter between the bottom and top diameters of 5m and 3m, respectively. The OWTs are installed on 6m diameter monopile foundations (this value is used for calculating the wave load on the substructure). The natural frequency is also necessary for the calculation of dynamic amplification factors and it is estimated as 0.335Hz following [11]. (The data are summarised in Table 1.)

Turbine data	
Turbine type:	Siemens SWT-3.6-107
Turbine Power:	*3.6 MW*
Turbine rotational speed:	*5-13 rpm*
Operational wind speed range	*4-25 m/s*
Number of blades	*3*
Tower and Support Structure data	
Hub height from Mean Sea Level:	$H = 83.5\ m$
Tower top diameter:	$D_t = 3\ m$
Tower bottom diameter	$D_b = 5\ m$
Monopile/substructure diameter:	$D_P = 6\ m$
Rotor and Blade data	
Turbine rotor diameter:	$D = 107\ m$
Rotor overhang	$b = 4\ m$
Blade root diameter	$B_{root} = 4\ m$
Blade tip chord length	$B_{tip} = 1\ m$
Blade length	$L = 52\ m$
Site Data	
Mean Sea Depth:	*21.5 m*
Average distance from closest shore:	*19 km*
Yearly mean wind speed	*9 m/s*
Dominant wind direction:	*West/South-West*
Estimated fetch:	*60 km*

Table 1 – Relevant data of the Siemens SWT-3.6-107 wind turbine and the Walney 1 site

3.2 Wind Load Spectrum

The wind moment spectrum is given by Equation 11. To construct the moment, one needs the diameter of the rotor ($D = 107\ [m]$), density of air $\rho_a = 1.225\ [kg/m^3]$, hub height $H = 83.5\ [m]$, mean sea level ($MSL = 21.5\ [m]$). The mean wind speed is taken as the yearly mean wind speed at the site $\overline{U} = 9\ [m/s]$, and this way the thrust coefficient $C_T = 7/\overline{U} = 7/9\ [-]$and the standard deviation of wind speed $\sigma_U = I\overline{U}$ can be calculated. The Kaimal spectrum is constructed using the standard value of the integral length scale as given in the DNV code [6]) $L_k = 340.2\ [m]$:

$$\tilde{S}_{uu}(f) = \frac{\frac{4L_k}{\overline{U}}}{\left(1+\frac{6fL_k}{\overline{U}}\right)^{\frac{5}{3}}} = \frac{\frac{4\cdot 340.2}{9}}{\left(1+\frac{6\cdot 340.2f}{9}\right)^{\frac{5}{3}}} = \frac{1360.8}{\overline{U}\left(1+\frac{2041.2f}{\overline{U}}\right)^{\frac{5}{3}}} \tag{35}$$

The turbulence intensity I can be calculated using the Normal Turbulence Model (NTM) as described in IEC 61400-1 [19] or the modified formulae for offshore environments given in IEC-61400-1 [26]. The three classes A,B and C given in IEC 61400-1 have decreasing reference turbulence intensities of 16%, 14% and

12%, respectively. The reference turbulence intensity refers to the expected value of the turbulence intensity at hub height at a 10 minutes mean wind speed of 15 [m/s]. The turbulence standard deviation is calculated as

$$\sigma_U = I_{ref}(0.75\overline{U} + b) \quad \text{with} \quad b = 5.6\ \left[\frac{m}{s}\right] \tag{36}$$

and with σ_U the turbulence intensity is calculated as $I = \sigma_U/U$. For offshore conditions in absence of site-measured data, the turbulence standard deviation is calculated from the surface roughness z_0, which is determined from the following implicit expression:

$$z_0 = \frac{A_C}{g}\left[\frac{\kappa\overline{U}}{\ln\left(\frac{H}{z_0}\right)}\right]^2 \tag{37}$$

where z_0 is the surface roughness, A_C is the Charnock's constant with $A_C = 0.011$ for open sea and $A_C = 0.034$ for near shore sites. κ=0.4 is von Kármán's constant, g is the gravitational constant, H is the hub height above sea level, and $\overline{U}$ is the mean wind speed. Using the value of z_0 the turbulence standard deviation is determined by:

$$\sigma_U = \frac{\overline{U}}{\ln\left(\frac{H}{z_0}\right)} + 1.28 \cdot 1.44 \cdot I_{ref} \quad \text{with} \quad I = \sigma_U/\overline{U} \tag{38}$$

The turbulence intensity curves for the three wind turbine classes A, B, C as well as the modified offshore curves for near-shore (1) and open sea (2) locations are given in Figure 14. It is to be noted that offshore turbulence intensities are lower than those onshore, however, at high wind speeds it remains steady and even an increase in turbulence is seen at very high wind speeds (>25[m/s]). This was also observed in measurements in e.g. [52], [53].

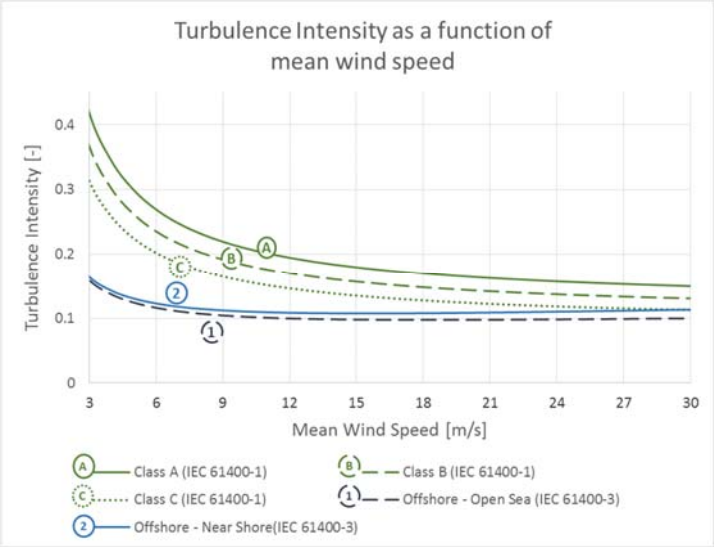

Figure 14. Turbulence for the three wind turbine classes A, B and C following and for offshore wind turbines in near-shore (1) and open sea (2) locations as a function of the 10-minutes mean wind speed.

Here the offshore near-coastal formula (Equation 38 with $A_C = 0.034$) is used, with which the mudline moment spectrum can be written substituting into Equation 11 and using Equation 2 as:

$$S_{MM,wind} = \frac{7.28{\cdot}10^{16}{\cdot}\overline{U}{\cdot}[I(\overline{U})]^2}{\left(1+\frac{2041.2f}{\overline{U}}\right)^{\frac{5}{3}}} \tag{39}$$

The mudline moment spectrum is plotted in Figure 15 for $\overline{U} = 9\ [m/s]$, curve (4) without and curve (3) with dynamic amplification factor included. The fore-aft bending moment at mudline due to turbulence is approximated by Equations 1, 3-4, and 7, using the standard deviation as the fluctuating component of wind speed. The static component is calculated from Equation 4 using the mean wind speed. In the Kaimal spectrum, most of the power is concentrated in the very low frequencies therefore the dynamic part of the loading is approximated by placing the total standard deviation of the bending moment, which is the integral under the spectrum curve, at the peak frequency $f_p = 0.0017\ [Hz]$. Table 2 shows the calculated forces and moments for several different mean wind speeds. The dynamic amplification factor is about 1 for such low frequency excitations.

Wind speed $\overline{U}[m/s]$	Thrust force on the hub, static wind load $Th_{stat}[MN]$	Thrust force on the hub, dynamic wind load $Th_{dyn}[MN]$	Fore-aft bending moment at mudline level,static wind moment $M_{wind,stat}[MNm]$	Fore-aft bending moment at mudline level, dynamic wind load moment $M_{wind,dyn}[MNm]$
5	0.193	0.050	20.24	5.25
9	0.347	0.078	36.43	8.19
15	0.578	0.124	60.72	13.02
20	0.771	0.213	80.96	22.365

Table 2 – Wind loading (static and fluctuating components) for several wind speed values

3.3 Wave Load Spectrum

The wave load spectrum is given by Equation 22. To construct the spectrum, one needs the inertia coefficient of the substructure $C_m = 2$ (based on [6]), the density of sea water$\rho_w = 1030\ [kg/m^3]$, the diameter of the substructure $D_P = 6\ [m]$, the mean sea depth $S = 21.5\ [m]$, and the wave number k. The latter can be determined from the dispersion relation (Equation 12), using the angular frequency of the waves. The deep water assumption $\lambda < 2S$ does not hold for all important frequencies at the Walney site. The JONSWAP spectrum can be determined as shown in Equation 13. The fetch is estimated at $F = 60\ [km]$, the mean wind speed is $\overline{U} = 9\ [m/s]$, the intensity of spectrum is $\alpha = 0.011$, the peak enhancement factor is $\gamma = 3.3$ and the peak frequency is $f_p = 0.197\ [Hz]$, the spectrum is given as:

$$S_{ww}(f) = \frac{6.8 \cdot 10^{-4}}{f^5} e^{-\frac{5}{4}\left(\frac{0.197}{f}\right)^4} \gamma^r$$
$$r = e^{-\frac{(f-0.197)^2}{0.0776\sigma^2}} \quad \sigma = \begin{cases} 0.07 & f \le f_p \\ 0.09 & f > f_p \end{cases} \tag{40}$$

The mudline moment spectrum can be numerically calculated, and is presented in Figure 15, in curve (2) without and in curve (1) with dynamic amplification factor included. The magnitude of the mudline bending moment due to wave loading is estimated for several wind speeds using a single linear wave approximation of the spectrum. The significant wave height $H_{1/3}$ and peak wave period T_p are determined from the JONSWAP spectrum using Equations 17-18. The moment load is calculated by Equations 20. The horizontal wave force can be calculated as:

$$F_{T,max} = M_{I,max} = \int_{-S}^{\eta} dF_{I,max} dz \tag{41}$$

with $\eta = 0$ one can write

$$F_{T,max} = C_m \rho_w \frac{D_P^2 \pi^3}{2} \frac{H_{1/3}}{T^2 \sinh(kS)} \int_{-S}^{0} \cosh(k(S+z)\,)\, dx = C_m \rho_w \frac{D_P^2 \pi^3}{2} \frac{H_{1/3}}{T^2 k} \qquad (42)$$

The results for the significant wave height, peak wave period and force and bending moment loads for some wind speed values are shown in Table 3. The dynamic amplification factors (DAF) along with the increased dynamic loads are also given in the table.

Wind speed $\bar{U}[m/s]$	Significant wave height $H_{1/3}[m]$	Peak wave period $T_p[s]$	Peak frequency $f_p[Hz]$	DAF [-]	Horizontal wave force, dynamic component $F_T[MN]$ / (with DAF)	Mudline moment, dynamic component $M_T[MNm]$ / (with DAF)
5	0.64	4.17	0.240	2.03	0.146 / (0.296)	3.15 / (6.39)
9	1.15	5.08	0.197	1.52	0.328 / (0.499)	5.1 / (7.76)
15	2.05	6.02	0.166	1.32	0.540 / (0.7128)	7.6 / (10.06)
20	2.56	6.62	0.151	1.25	0.706 / (0.8825)	9.45 / (11.84)

Table 3 – Wave parameters and wave loading for several wind speed values

3.4 1P loading

To determine the 1P moment spectrum one needs a typical value of the mass imbalance of the rotor. Some values are available for a somewhat smaller wind turbine studied in [21] and [20]. For the 2MW Vestas V80 turbine mass imbalance values of about 350-500 [kgm] were applied in these studies. The imbalance value is estimated for the 3.6MW Siemens wind turbine by assuming that the imbalance is proportional to the mass of the rotor and also to the diameter of the turbine. The mass ratio and the diameter ratio of the rotors are calculated and the imbalance is scaled up by both ratios. The mass of the rotor of the Vestas turbine is 37.5 tonnes [54], while that of the Siemens turbine is 95 tonnes [49]. The diameter of the Vestas turbine's rotor is 80m and that of the Siemens turbine is 107m. Therefore, the estimated imbalance value for the Siemens SWT-107-3.6 turbine is estimated as shown in Equation 41.

$$I_{m,SWT107} = I_{m,V80} \cdot \frac{M_{SWT107}}{M_{V80}} \cdot \frac{D_{SWT107}}{D_{V80}} = 500 \cdot \frac{95}{37.5} \cdot \frac{107}{80} \approx 1694\ [kg \cdot m] \qquad (43)$$

The original imbalance value of the V80 is a value typical for an average operational wind turbine. As an upper bound estimate one may consider $I_m = 2000\ [kgm]$.The distance between the axis of the tower and the centre of the hub (i.e. the rotor overhang) is estimated as $b = 4\ [m]$. (For clarity, see Figure 13.) This way the maximum of the fore-aft bending moment caused by the imbalance is written as:

$$M_{1P} = 4 \cdot 4\pi^2 \cdot 2000 \cdot f^2 = 3.1583 \cdot 10^5 \cdot f^2 \qquad (44)$$

The maximum bending moment occurs at the highest rotational speed of $\Omega = 13\ [rpm]$, that is $f = 0.2167\ [Hz]$, its value is $M_{1P} = 0.015\ [MNm]$. The spectrum of the 1P loading is a Dirac-delta function as described in Section 2.3. Figure 15 shows the 1P loading in the fore-aft direction as a function of the Hertz frequency of the rotation f, in curve (5) with dynamic amplification and in curve (6) without DAF. Even though the side-to-side direction is not considered in this paper, it is important to mention that the 1P side-to-side mudline bending moments are significantly higher than the fore-aft components. This is because of the large lever arm of the force i.e. the distance between the hub height and the mudline $(H + MSL)$. Figure 15 also plots the side-to-side 1P mudline bending moment as a function of the Hertz frequency of rotation, in curve (9) with and in curve (10) without dynamic amplification. The low value of modal damping of 0.5% was used, which is due is due to low aerodynamic damping in the side-to-side mode (cross-wind direction), as discussed in Section 2.7. This results in higher dynamic amplification factors of the response in the side-to-side vibration mode. Table 4 shows the values of 1P fore-aft and side-to-side moments from the imbalance. It can be seen that after reaching the rated rotational speed of 13rpm (at about 14 m/s), the 1P load does not increase.

Mean wind speed at hub height $\bar{U}[m/s]$	Rotational speed $\Omega\ [rpm]$	Fore-aft DAF [-]	1P fore-aft mudline bending moment $M_{1P}[MNm]$ / (with DAF)	Side-to-side DAF [-]	1P side-to-side mudline bending moment $M_{1P,side-to-side}[MNm]$ / (with DAF)
5	5.8	1.09	0.002 / (0.002)	1.09	0.077 / (0.084)
9	9	1.25	0.007 / (0.009)	1.25	0.187 / (0.234)
15	13	1.71	0.015 / (0.025)	1.72	0.389 / (0.669)
20	13	1.71	0.015 / (0.025)	1.72	0.389 / (0.669)

Table 4 – 1P fore-aft and side-to-side moments for several values of wind speed

3.5 3P loading

The 3P moment can be determined by estimating the total drag moment on the top part of the tower which is covered by the downward pointing blade and then reducing this moment by the ratio of the face area of the blade and the face area of the top part of the tower. The drag moment is estimated by the method presented in Section 2.4. The density of air is $\rho_a = 1.225\ [kg/m^3]$, the drag coefficient of the tubular tower at high Reynolds number is $C_D \approx 0.5\ [-]$, the linearly decreasing diameter of the tower can be written as:

$$D(z) = D_b - (D_b - D_t)\cdot\frac{z}{H} = 5 - 2\cdot\frac{z}{83.5} \tag{45}$$

with the z coordinate running from mean sea level along the length of the tower, D_b and D_t are the bottom and top diameters of the tower, respectively. Using the exponential wind profile and the water depth $S = 21.5\ [m]$, the moment can be written as:

$$M_{towertop} = 0.306\bar{U}^2\int_{31.5}^{83.5}\left(5 - 2\cdot\frac{z}{83.5}\right)z^{2/7}(z+21.5)dx = 4019\cdot\bar{U}^2\ [Nm] \tag{46}$$

which gives $M_{drag} \approx 0.326[MNm]$ for $\bar{U} = 9\ [m/s]$. Both the area of the blade and the area of the top part of the tower are approximated as trapezoids, the areas are calculated as:

$$\begin{aligned} A_{blade} &= \frac{(d_{root} + d_{tip})}{2}L = \frac{4+1}{2}\cdot 52 = 130\ [m^2] \\ A_{towertop} &= \frac{D_{lower} + D_{top}}{2}L = \frac{4.25+3}{2}\cdot 52 = 188.2[m^2] \end{aligned} \tag{47}$$

The magnitude of the load loss is then approximated as written in Equation 45.

$$M_{3P} = M_{towertop}\frac{A_{blade}}{A_{towertop}} = 0.326\cdot\frac{130}{188.2}[MNm] = 0.225[MNm] \tag{48}$$

The drag load on the tower is calculated by integrating along the whole tower:

$$M_{drag} = \int_0^H \frac{1}{2}\rho_a C_D D(z)U(z)^2(z+S)dz \qquad F_{drag} = \int_0^H \frac{1}{2}\rho_a C_D D(z)U(z)^2 dz \tag{49}$$

The 3P forces and moments are estimated in Table 5 for several values of the mean wind speed. Note that in the vicinity of 6.125 m/s (~6.7rpm rotational speed) the DAF gets very high and the 3P moment is an order of magnitude higher than without DAF. In Figure 15 the 3P mudline moment squared is shown with and without DAF in curve (7) and curve (8), respectively. It can be seen that after reaching the maximum rotational speed (13 rpm) at the mean wind speed of 14 m/s, the load keeps increasing as the tower drag increases, but the frequency of excitation remains constant at the 3P value corresponding to 13 rpm $f_{3P@13rpm} = 0.65\ Hz$ (vertical section in Figure 15).

Wind speed $\bar{U}[m/s]$	Total drag force on the tower $[MN]$	Total drag moment on the tower $[MNm]$	3P freq. [Hz]	DAF [-]	3P force $F_{3P}[MN]$ / (with DAF)	3P moment $M_{3P}[MNm]$ / (with DAF)
5	0.0019	0.176	0.29	3.77	0.001 / (0.003)	0.069 / (0.262)
9	0.0062	0.570	0.45	1.23	0.003 / (0.004	0.225 / (0.275)
15	0.0173	1.584	0.65	0.36	0.008 / (0.003)	0.625 / (0.225)
20	0.0308	2.816	0.65	0.36	0.014 / (0.005)	1.111 / (0.401)
6.125 (resonance)	0.0289	0.189	0.335	10	0.001/ (0.013)	0.104 / (1.042)

Table 5 – 3P loading and drag load on the tower

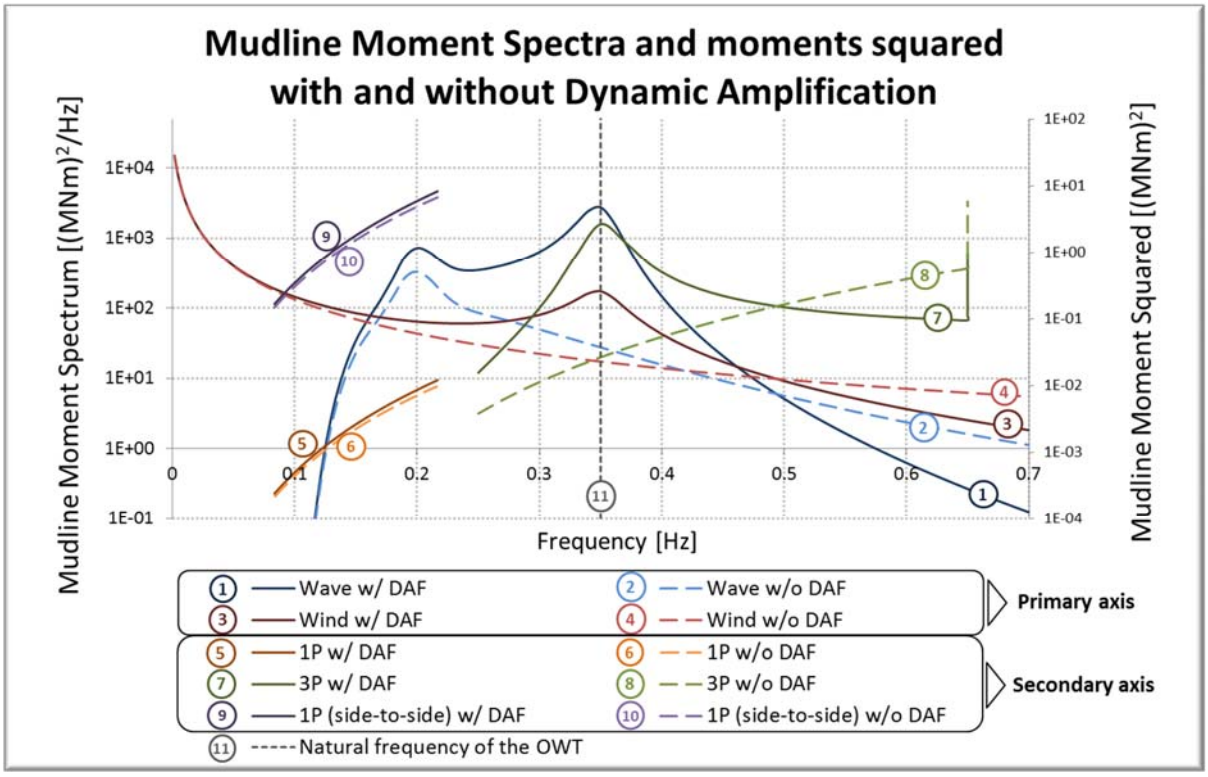

Figure 15: Fore-aft bending moment spectrum at mudline – Siemens SWT-3.6-107 at the Walney 1 wind farm. The amplitudes of the 1P and 3P moment squares are to be compared to the integral under the wind and wave spectrum curves, not directly to the spectra.

3.6 Summary of loads and comparison

The static and dynamic loads are summarised in Table 6 for two different wind speeds with dynamic loads in bold font. For the sake of completeness static current load is included in the table. The current load can be calculated as a drag force on the substructure using Morison's equation (see Equation 14). Data about the current and tidal stream conditions at the Walney site are not available, however, using the tidal atlas of the Irish Sea available on the internet at www.visitmyharbour.com [55] one can see that the tidal stream velocity rarely exceeds 1 knot (approximately 0.514 m/s). Using this value, Morison's equation estimates a static

force of 0.0176MN and a static mudline bending moment of 0.189MNm due to currents acting on the substructure. The effect of dynamic amplification on the spectra is shown in Figure 15 and the effect on the 1P and 3P loads is shown in Figure 16.

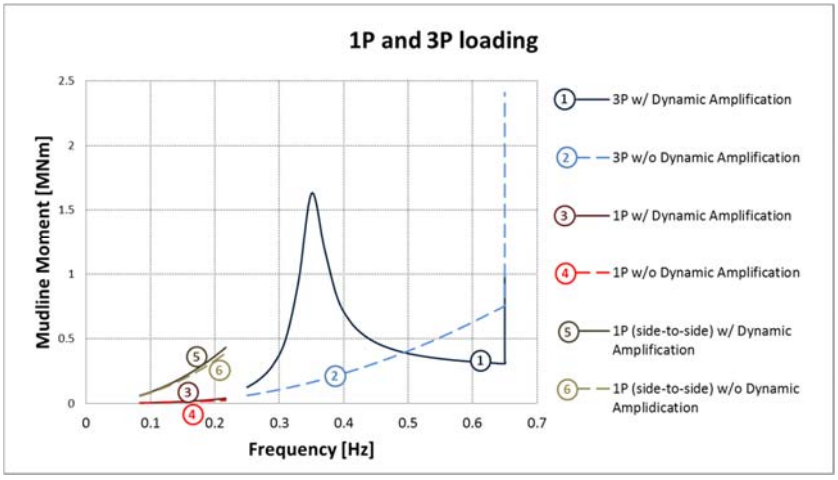

Figure 16: 1P fore-aft bending moment, 1P side-to-side bending moment and 3P bending moment at mudline with and without dynamic amplification.

Load	$\bar{U} = 9\ [m/s]$		$\bar{U} = 20\ [m/s]$	
	Fore-aft bending moment [MNm] / (w/ DAF)	Force (parallel to axis x) [MN] (w/ DAF)	Fore-aft bending moment [MNm] (w/ DAF)	Force (parallel axis x) [MN] (w/ DAF)
Wind load (static)	36.4	0.35	80.96	0.771
Wind load (dynamic)	**12.6 (12.6)**	**0.12 (0.12)**	**27.98**	**0.27 (0.27)**
Current/tidal stream	0.19	0.018	0.19	0.018
Wave loading	**5.1 (7.76)**	**0.33 (0.50)**	**9.45 (11.84)**	**0.71 (0.88)**
1Ploading	**0.01 (0.01)**	-	**0.025 (0.043)**	-
(3P loading)	*0.225 (0.275)*	*0.003 (0.004)*	*1.11 (0.40)*	*0.014 (0.005)*
Tower drag (static)	0.57	0.006	2.82	0.031
Total static load	37.2	0.37	84.0	0.82
Total dynamic load	**17.7 (20.4)**	**0.45 (0.62)**	**37.5 (39.9)**	**0.97 (1.15)**
Total maximum load	54.9 (57.6)	0.82 (0.99)	121.5 (123.9)	1.79 (1.97)

Table 6 – Estimated static and dynamic loads (values with dynamic amplification in brackets). The wind load was calculated using the peak frequency of 0.0017[Hz], therefore the dynamic amplification factor (DAF) is 1 for the wind loading. The total static load is calculated as the sum of the static wind load, the current load and the tower drag load. The total dynamic load is calculated as the sum of the dynamic wind load, the wave loading, and the 1P loading. The 3P cyclic loading is basically a load loss, therefore it is not to be added.

The theoretical wave moment spectrum matches well the spectrum obtained as a result of 500 time simulations reported in [36]. It is to be noted that the peak frequency of the JONSWAP spectrum of waves is significantly (two orders of magnitude) higher than that of the Kaimal spectrum of wind. This means significantly higher cycle count of wave loading than that of wind loading during the lifetime of the turbine. The estimated magnitudes of static and dynamic loads are comparable with the estimations of Byrne and

Houlsby [56]. However, the wave loads are significantly lower, since the wind farm location in the Irish Sea is somewhat sheltered and the fetch is limited, therefore very high waves do not commonly develop.

3.7 Limitations

The methodology presented in this study provides mudline moment spectra as a basis for frequency based fatigue damage estimation. As a tool for the early design phase, the methodology has limitations that are important to note and are listed below:

(a) The analysis takes into account only the power production stage of the wind turbine. However, fatigue damage also occurs during start-up, shutdown, parked state and other scenarios. The mudline bending moment spectra were calculated using theoretical spectra, Kaimal spectrum and JONSWAP spectrum for the wind and wave loading, respectively. It is important to note that these spectra are not calculated as "lifetime representative" spectra but rather correspond to a certain set of environmental conditions (i.e. certain sea state and wind conditions). The spectra can be calculated for different environmental conditions using the given formulae; different conditions occur with different probability. From the point of view of fatigue damage, the assumed aerodynamic admittance function of $\chi(f) = 1$ as given in Section 2.2 provides a conservative estimation for each set of conditions. The design standards encourage the use of site specific spectra wherever available.

(b) Due to long term wind speed variations, the static component of the wind produces stress cycles with high amplitude but low frequency. Even though the number of cycles for these loads is much lower than for the loads addressed in this study, the high amplitudes may contribute significantly to the fatigue damage.

(c) The quasi-steady approximation of wind speed fluctuations gives a rough estimation of the fluctuating wind load. The present formulation is a simplified tool to precede detailed time domain analysis. For detailed fatigue analysis a non-linear time domain approach like the Blade Element Momentum (BEM) theory ([28], [15]) is more suitable. However, the BEM method requires a significant amount of information about the blade design as well as a detailed description of the aerofoil characteristics of each radial section.

(d) The proposed formulation assumes collinear wind and wave directions, i.e. that there is no misalignment between the wind speed and the propagation direction of waves. This is often true for winds blowing onshore, but not common for winds blowing offshore. This means that the estimation given by summing the individual contributions is a conservative upper bound estimate of the fatigue. The IEC standards [19], [26] require the wind turbines to operate with yaw error, the present approach using Figure 6 and Equation 7 can be considered conservative for yawed flow.

(e) The simplistic formula for the thrust coefficient shown in Equation 9 is a rough upper bound estimate which was tested for several wind turbines in the original work [30]. The thrust coefficient of the wind turbine can be calculated more accurately applying the BEM Theory (or other more refined methods).

(f) The estimation of fetch is an uncertain process and the resulting wave heights and wave periods should be compared to typical values at a given site. Alternatively, the formulation based on $H_{1/3}$ and T_p given in Equation 26 may be used. The first order Airy wave approximation of the wave particle kinematics is only valid for deeper waters, and it may be necessary to use higher order methods. Very high nonlinear waves and severe wave impacts caused by breaking waves occur rarely and thus have low cycle numbers but high load magnitude and may contribute significantly to the fatigue damage.

(g) The derivations were carried out for three bladed wind turbines because they are dominating the offshore wind industry. However, the calculation methods are similar for two bladed turbines as well. For the same rotational speed range, the 1P-2P gap is smaller than the 1P-3P gap, although 2 bladed turbines tend to spin somewhat faster.

(h) It is to be noted that Morison's equation as discussed in Section 2.4 is developed for slender piles, and typically suitable for jacket structural components and monopiles. However, when the structure is large (as compared to the typical wave lengths) and the foundation disturbs the wave kinematics, such as in case of gravity base foundations Morison's method is not sufficient, and wave diffraction analysis has to be carried out [6]. Different methods are summarised in the OWTES Project report [25], where Morison's method, diffraction models, Froude-Krylov/Pressure Integration methods and CFD are compared in terms of applicability, ease of use and calculation speed.

(i) The two spectra can be superposed by simply summing the moment spectra from wind and waves:

$$S_{MM,total} = S_{MM,wind} + S_{MM,waves} \quad (50)$$

If safety factors (load factors) γ are to be included as suggested in DNV-OS-J101 [6] the load factors are to be squared for the spectra, that is

$$S_{MM,total} = \gamma_{wind}^2 S_{MM,wind} + \gamma_{wave}^2 S_{MM,waves} \quad (51)$$

(j) The calculated mudline bending moment spectrum may be used to calculate fatigue damage using frequency domain methods, such as Dirlik's method [57], Tovo-Benasciutti methods [58], $\alpha_{0.75}$ method [59], Gao-Moan method [60] and many more. Validation of the methodology on load time histories from different offshore wind farm sites with known characteristics is necessary, however, there are very limited measurement data available in the public domain.

4. Discussion and Conclusions

In this study an attempt has been made to provide a quick and simple methodology to estimate the fore-aft mudline bending moment spectra of offshore wind turbines for the four main types of dynamic loads: wind, wave, rotor mass imbalance (1P), and blade passage (3P). An example calculation is presented for an operational industrial Siemens SWT-107-3.6 wind turbine at the Walney 1 site and the mudline moment spectra are plotted (taking into account dynamic amplifications).

The motivation behind this simplified methodology is to provide a basis for a quick frequency domain fatigue damage estimation in the preliminary design phase of these structures which is otherwise a very lengthy process usually done in time domain. This would also encourage integrated design of OWTs incorporating the dynamics and fatigue analysis in the early stages of structural design. Therefore, it was also an objective to use as little site specific information of the wind turbine as possible. Information such as the control parameters, the blade design, aerofoil characteristics, generator characteristics, etc. are not necessary in this formulation. It must be mentioned here that the description and comparison of the most important frequency domain fatigue damage estimation methods are available in a recent literature review [61].

References

[1] S. Bhattacharya, D. Lombardi, and D. Muir Wood, "Similitude relationships for physical modelling of monopile-supported offshore wind turbines," *Int. J. Phys. Model. Geotech.*, vol. 11, no. 2, pp. 58–68, Jun. 2011.

[2] S. Bhattacharya, J. a. Cox, D. Lombardi, and D. M. Wood Muir Wood, "Dynamics of offshore wind turbines supported on two foundations," *Proc. ICE - Geotech. Eng.*, vol. 166, no. 2, pp. 159–169, Apr. 2013.

[3] S. Bhattacharya, N. Nikitas, J. Garnsey, N. A. Alexander, J. Cox, D. Lombardi, D. Muir Wood, and D. F. T. Nash, "Observed dynamic soil–structure interaction in scale testing of offshore wind turbine foundations," *Soil Dyn. Earthq. Eng.*, 2013.

[4] J. W. Cooley, P. A. W. Lewis, and P. D. Welch, "The Fast Fourier Transform and Its Applications," *IEEE Trans. Educ.*, vol. 12, no. 1, pp. 27–34, 1969.

[5] J. Apt, "The spectrum of power from wind turbines," *J. Power Sources*, vol. 169, pp. 369–374, 2007.

[6] DNV, "Offshore Standard DNV-OS-J101 - Design of Offshore Wind Turbine Structures," no. October, 2010.

[7] DNV/Risø, *Guidelines for Design of Wind Turbines*, 1st Editio., vol. W. DNV/Risø in technical co-operation, 2001.

[8] D. Kallehave and C. L. Thilsted, "Modification of the API p-y Formulation of Initial Stiffness of Sand," in *Offshore Site Investigation and Geotechnics: Integrated Geotechnologies - Present and Future*, 2012.

[9] S. Bhattacharya and S. Adhikari, "Experimental validation of soil–structure interaction of offshore wind turbines," *Soil Dyn. Earthq. Eng.*, vol. 31, no. 5–6, pp. 805–816, May 2011.

[10] D. Lombardi, S. Bhattacharya, and D. Muir Wood, "Dynamic soil–structure interaction of monopile supported wind turbines in cohesive soil," *Soil Dyn. Earthq. Eng.*, vol. 49, pp. 165–180, Jun. 2013.

[11] S. Adhikari and S. Bhattacharya, "Vibrations of wind-turbines considering soil-structure interaction," *Wind Struct.*, vol. 14, no. 2, pp. 85–112, 2011.

[12] S. Adhikari and S. Bhattacharya, "Dynamic analysis of wind turbine towers on flexible foundations," *Shock Vib.*, vol. 19, no. 1, pp. 37–56, 2012.

[13] M. Kühn, "Soft or stiff: A fundamental question for designers of offshore wind energy converters," in *Proc. European Wind Energy Conference EWEC '97*, 1997.

[14] C. Leblanc, “Design of Offshore Wind Turbine Support Structures - Selected topics in the field of geotechnical engineering,” Aalborg University, Denmark, 2009.
[15] T. Burton, N. Jenkins, D. Sharpe, and E. Bossanyi, *Wind energy handbook*. Chichester, West Sussex, England: John Wiley & Sons, Ltd, 2001.
[16] K. Hasselmann, T. P. Barnett, E. Bouws, H. Carlson, D. E. Cartwright, K. Enke, J. A. Ewing, H. Gienapp, D. E. Hasselmann, P. Kruseman, A. Meerburg, P. Müller, D. J. Olbers, K. Richter, W. Sell, and H. Walden, “Measurements of Wind-Wave Growth and Swell Decay during the Joint North Sea Wave Project (JONSWAP),” *Erganzungsh. zur Dtsch. Hydrogr. Zeitschrift*, vol. 46, no. 8 0, 1973.
[17] Germanischer Lloyd WindEnergie GmbH, “Guideline for the Certification of Offshore Wind Turbines,” 2005.
[18] DNV, “Recommended Practice DNV-RP-C205 - Environmental conditions and environmental loads,” no. October. DNV, 2010.
[19] IEC, “International Standard IEC-61400-1 Wind Turbines - Part 1: Design requirements, Third Edition,” vol. 2005. International Electrotechnical Commission (IEC), 2005.
[20] R. Ramlau and J. Niebsch, “Imbalance Estimation Without Test Masses for Wind Turbines,” *J. Sol. Energy Eng.*, vol. 131, no. 1, p. 11010, Jan. 2009.
[21] J. Niebsch, R. Ramlau, and T. T. Nguyen, “Mass and Aerodynamic Imbalance Estimates of Wind Turbines,” *Energies*, vol. 3, no. 4, pp. 696–710, Apr. 2010.
[22] G. I. Taylor, “The Spectrum of Turbulence,” *Proc. R. Soc. A Math. Phys. Eng. Sci.*, vol. 164, no. 919, pp. 476–490, Feb. 1938.
[23] D. Schlipf, D. Trabucchi, O. Bischoff, M. Hofsäß, J. Mann, T. Mikkelsen, A. Rettenmeier, J. J. Trujillo, and M. Kühn, “Testing of Frozen Turbulence Hypothesis for Wind Turbine Applications with a Scanning LIDAR System,” in *15th International Symposium for the Advancement of Boundary Layer Remote Sensing*, 2010, no. 3.
[24] E. L. Petersen, N. G. Mortensen, L. Landberg, J. Hùjstrup, and H. P. Frank, “Wind Power Meteorology . Part I : Climate and Turbulence,” vol. 45, pp. 25–45, 1998.
[25] T. R. Camp, M. J. Morris, R. van Rooij, J. van der Tempel, M. Zaaijer, A. Henderson, K. Argyriadis, S. Schwartz, H. Just, W. Grainger, and D. Pearce, “Design Methods for Offshore Wind Turbines at Exposed Sites (Final Report of the OWTES Project EU Joule III Project JOR3-CT98-0284),” Bristol, 2004.
[26] IEC, *International Standard IEC 61400-3 Wind turbines - Part 3: Design requirements for offshore wind turbines*, 1.0 ed. International Electrotechnical Commission (IEC), 2009.
[27] I. Van der Hoven, “Power spectrum of horizontal wind speed in the frequency range from 0.0007 to 900 cycles per hour,” *J. Meteorol.*, vol. 14, 1957.
[28] M. O. L. Hansen, *Aerodynamics of Wind Turbines*, Second Edi. Earthscan, 2008, pp. 147–156.
[29] P. S. Veers, “Three-Dimensional Wind Simulation,” Report prepared by Sandia National Laboratories, Albaquerque, New Mexico, 1988.
[30] P. Frohboese and C. Schmuck, “Thrust coefficients used for estimation of wake effects for fatigue load calculation,” in *European Wind Energy Conference 2010, Warsaw, Poland*, 2010, pp. 1–10.
[31] IEC, “International Standard IEC-61400-1 Amendment 1 - Wind turbines - Part 1: Design requirements, 3rd Edition.” International Electrotechnical Commission (IEC), 2009.
[32] R. H. Stewart, *Introduction To Physical Oceanography*, no. September. Department of Oceanography, Texas A & M University, 2008.
[33] W. J. Pierson and L. Moskowitz, “A proposed spectral form for fully developed wind seas based on the similarity theory of S. A. Kitaigorodskii,” *J. Geophys. Res.*, vol. 69, no. 24, pp. 5181–5190, Dec. 1964.
[34] G. B. Whitham, *Linear and Nonlinear Waves*, vol. 28, no. 6. John Wiley & Sons, Ltd, 1974, pp. 471–476.
[35] R. G. Dean, “Stream Function Representation of Nonlinear Ocean Waves,” *J. Geophys. Res.*, vol. 70, no. 18, pp. 4561–4572, 1965.
[36] M. van der Meulen and T. Ashuri, “Influence of Nonlinear Irregular Waves on the Fatigue Loads of an Offshore Wind Turbine,” *lr.tudelft.nl*., n.d.,
[37] H. F. Veldkamp and J. van der Tempel, “Influence of wave modelling on the prediction of fatigue for offshore wind turbines,” *Wind Energy*, vol. 8, no. 1, pp. 49–65, Jan. 2005.
[38] J. R. Morison, J. W. Johnson, and S. A. Schaaf, “The Force Exerted by Surface Waves on Piles,” *J. Pet. Technol.*, vol. 2, no. 5, pp. 149–154, May 1950.
[39] A. R. Henderson, M. B. Zaaijer, and T. R. Camp, “Hydrodynamic Loading on Offshore Wind Turbines,” in Proceedings of the Offshore Windenergy in Mediterranean and Other European Seas (OWEMES conference), Naples, Italy, 2003
[40] M. Ozbek and D. J. Rixen, “Operational modal analysis of a 2.5 MW wind turbine using optical measurement techniques and strain gauges,” Wind Energy, vol. 16, no. 3, pp. 367–381, Apr. 2013.
[41] D. Salzmann and J. van der Tempel, “Aerodynamic damping in the design of support structures for offshore wind turbines,” *Pap. Copenhagen Offshore Wind 2005*, 2005.
[42] J. M. Jonkman and M. L. Buhl Jr, “FAST User’s Guide (Technical Report),” National Renewable Energy Laboratory, Golden, Colorado, US, 2005.

[43] M. H. Hansen, K. Thomsen, P. Fuglsang, and T. Knudsen, “Two methods for estimating aeroelastic damping of operational wind turbine modes from experiments,” *Wind Energy*, vol. 9, no. 1–2, pp. 179–191, Jan. 2006.
[44] P. J. Murtagh, a. Ghosh, B. Basu, and B. M. Broderick, “Passive control of wind turbine vibrations including blade/tower interaction and rotationally sampled turbulence,” *Wind Energy*, vol. 11, no. 4, pp. 305–317, Jul. 2008.
[45] M. Damgaard and J. Andersen, “Natural frequency and damping estimation of an offshore wind turbine structure,” in *Proceedings of the Twenty-second (2012) International Offshore and Polar Engineering Conference*, 2012, vol. 4, pp. 300–307.
[46] N. J. Tarp-johansen, D. Energy, A. C. M. Vænge, K. Sv, L. Andersen, and C. Mørch, “Comparing Sources of Damping of Cross-Wind Motion,” in *Proceedings of the European Offshore Wind Conference 2009*, Stockholm, Sweden, 2009.
[47] W. G. Versteijlen, A. V. Metrikine, H. J. S., and W. E. de Vries, “Estimation of the vibration decrement of an offshore wind turbine support structure caused by its interaction with soil,” in *Proceedings of the EWEA Offshore Conference*, Amsterdam, The Netherlands, 2011.
[48] M. Damgaard, L. B. Ibsen, L. V. Andersen, and J. K. F. Andersen, “Cross-wind modal properties of offshore wind turbines identified by full scale testing,” *J. Wind Eng. Ind. Aerodyn.*, vol. 116, pp. 94–108, May 2013.
[49] Siemens AG, “Brochure of the Siemens Wind Turbine SWT-3.6-107,” 2011. [Online]. Available: http://www.energy.siemens.com/us/pool/hq/power-generation/renewables/wind-power/wind turbines/E50001-W310-A103-V6-4A00_WS_SWT_3_6_107_US.pdf. [Accessed: 19-Aug-2013].
[50] DONG Energy, “Walney Offshore Wind Farm - Facts of the project,” 2013. [Online]. Available: http://www.dongenergy.com/walney/about_walney/about_the_project/pages/facts.aspx. [Accessed: 06-May-2013].
[51] Lindoe Offshore Renewables Center, “Walney 1 Offshore Wind Farm,” *lorc.dk*, 2013. [Online]. Available: http://www.lorc.dk/offshore-wind-farms-map/walney-1. [Accessed: 06-May-2013].
[52] H. Wang, R. Barthelmie, S. Pryor, and H. Kim, “A new turbulence model for offshore wind turbine standards,” *Wind Energy*, 2014.
[53] M. Türk and S. Emeis, “The dependence of offshore turbulence intensity on wind speed,” *J. Wind Eng. Ind. Aerodyn.*, vol. 98, no. 8–9, pp. 466–471, Aug. 2010.
[54] Vestas, “Brochure of the Vestas V80-2MW Wind Turbine,” 2003. [Online]. Available: www.vestas.com. [Accessed: 01-Oct-2013].
[55] www.visitmyharbour.com, “Hourly tidal streams Irish Sea and Bristol Channel,” *www.visitmyharbour.com*, 2013. [Online]. Available: http://www.visitmyharbour.com/articles/3180/hourly-tidal-streams-irish-sea-and-bristol-channel. [Accessed: 12-Oct-2013].
[56] B. W. Byrne and G. T. Houlsby, “Foundations for offshore wind turbines.,” *Philos. Trans. A. Math. Phys. Eng. Sci.*, vol. 361, no. 1813, pp. 2909–30, Dec. 2003.
[57] T. Dirlik, “Application of computers in fatigue analysis,” PhD Thesis, The University of Warwick, 1985.
[58] D. Benasciutti and R. Tovo, “Spectral methods for lifetime prediction under wide-band stationary random processes,” *Int. J. Fatigue*, vol. 27, no. 8, pp. 867–877, Aug. 2005.
[59] D. Benasciutti, “Fatigue analysis of random loadings,” PhD Thesis, University of Ferrara, 2004.
[60] Z. Gao and T. Moan, “Frequency-domain fatigue analysis of wide-band stationary Gaussian processes using a trimodal spectral formulation,” *Int. J. Fatigue*, vol. 30, no. 10–11, pp. 1944–1955, Oct. 2008.
[61] M. Mršnik, J. Slavič, and M. Boltežar, “Frequency-domain methods for a vibration-fatigue-life estimation – Application to real data,” *Int. J. Fatigue*, vol. 47, pp. 8–17, Feb. 2013.